Smart4RES

Report on improved NWP with higher spatial and temporal resolution

D2.2 Report on improved NWP with higher spatial and temporal resolution

WP2, T2.2

Version V3.0

Authors: Bastien Alonzo, Marie Cassas, Laure Raynaud, Météo-France

Remco Verzijlbergh, Daan Houf, Peter Baas, Brian Dsouza, Whiffle Weather Finecasting

Disclaimer

The present document reflects only the author's view. The European Climate, Infrastructure and Environment Executive Agency (CINEA) is not responsible for any use that may be made of the information it contains.

Technical references

Project Acronym	Smart4RES
Project Title	Next Generation Modelling and Forecasting of Variable Renewable Generation for Large-scale Integration in Energy Systems and Markets
Project Coordinator	ARMINES – MINES ParisTech
Project Duration	November 2019 – April 2023
Deliverable	D2.2: Report on improved Numerical Weather Prediction (NWP) with higher spatial and temporal resolution
Dissemination level [1]	PU
Nature [2]	R
Work Package	WP2 – Next generation of weather forecasting models for RES purpose
Task	T 2.2 – High-resolution NWP to meet RES needs
Lead beneficiary	Météo-France (MF)
Contributing beneficiary(ies)	ALL
Reviewers	Pierre Pinson (DTU), Dennis van der Meer (ARMINES)
Due date of deliverable	31 March 2022

[1]   PU = Public
        PP = Restricted to other program participants (including the Commission Services)
        RE = Restricted to a group specified by the consortium (including the Commission Services)
        CO = Confidential, only for members of the consortium (including the Commission Services)
[2]   R = Report, P = Prototype, D = Demonstrator, O = Other

Document history		
V	Date	Description
0.1	02/03/22	First draft submitted by Laure Raynaud
1.0	03/03/22	Review by Quentin Libois (WP leader)
2.0	16/03/22	Review by Pierre Pinson and Dennis van der Meer
3.0	07/04/22	Final public version released by Coordinator

Executive summary

Smart4RES is a research project funded under the H2020 programme. It aims to develop and validate next-generation of RES forecasting tools, enabling an increase of at least 15% in RES forecasting performance.

The work package 2 of Smart4RES is dedicated to *Next generation of weather forecasting models for RES purpose*. After a first deliverable D2.1 presenting the strategies considered within the project to improve the prediction of atmospheric variables relevant to RES forecasting using Numerical Weather Prediction (NWP) models, this document presents and discusses the added value of disruptive NWP forecasts with higher spatial and temporal resolutions.

This work is carried out by Météo-France and Whiffle. In Smart4RES, Météo-France developed an enhanced version of its operational ensemble system Arome-EPS over Europe, with a 1.3 km horizontal resolution and 5-minute temporal outputs (compared to the operational version with a 2.5 km resolution and 1-hour outputs). Focusing on 100-m wind speed and surface solar radiation, this high-resolution system is shown to increase the performance of RES-oriented variables and events (such as wind ramps) by about 3-4% on average.

In order to go deeper in the development of very high resolution NWP models, Whiffle ran state-of-the-art Large-Eddy-Simulations (LES) with the GRASP Model, including a direct modeling of wind farm effects. Comparison against ECMWF forecasts indicates a significant improvement for different use cases relevant for Smart4RES, which is mostly the consequence of GRASP's ability to represent a local wind climate better.

Table of contents

List of figures

Introduction

The development and advances of Numerical Weather Prediction (NWP) have certainly been the main factor of progress for improving weather forecasts and in particular the prediction of extreme events. NWP forecasts are also a key input to various weather-sensitive sectors such as agriculture, air traffic management or energy production. NWP models are constantly upgraded to improve the accuracy and timeliness of forecasts and alerts. A more precise   representation of the physical processes at play in the atmosphere, increase in spatial resolution and the use of new weather observations are the main avenues for further NWP improvements.

In this report we present the main impacts of enhanced NWP models specifically developed for the Smart4RES project by Météo-France and Whiffle, with a focus on increasing spatial and temporal resolutions. To this end, Météo-France's work is dedicated to high-resolution probabilistic forecasting using state-of-the-art Ensemble Prediction Systems. Another approach to numerical weather prediction is using Large-Eddy Simulation (LES), which differs from traditional NWP models on a number of aspects, but primarily in its treatment of turbulence and clouds. Whiffle has been pioneering the use of LES for operational weather forecasting since 2016 and is making use of graphics processing units (GPUs) to overcome the large computational cost associated with LES.

The assessment of Météo-France and Whiffle forecasts is performed on time periods and case studies relevant for Smart4RES. In addition, in order to develop NWP forecasts tailored to the RES sector, the forecast evaluation targets the users needs, with a focus on RES-oriented variables, primarily global horizontal irradiance (GHI) and 100-meter wind speed, and the development of user-oriented metrics such as wind ramps. The associated improvements are also quantified and compared to the projet KPI 1.1 : "i*mprovement in continuous ranking probability score (CRPS) around 4-6% for radiative variables and 5-10% for wind variables, compared to the baseline models, and for time horizons from few hours up to hundred hours-ahead".*

1.   High-resolution ensemble prediction

1.1 Presentation of ensemble forecasts

The intrinsic predictability of atmospheric dynamics, and in particular of small-scale phenomena such as those relevant for RES forecasting, is limited. In order to account for the uncertainty of weather forecasts it is now of common practice to use probabilistic forecasting, that aims at predicting the probability distribution of future atmospheric states, instead of a single deterministic weather forecast.

Probabilistic forecasting is currently implemented with Ensemble Prediction Systems (EPSs), that run in parallel multiple perturbed weather forecasts (also called "members"). Each forecast uses slightly different initial conditions, boundary conditions and model formulations in order to account for the different sources of uncertainty (Figure 1).
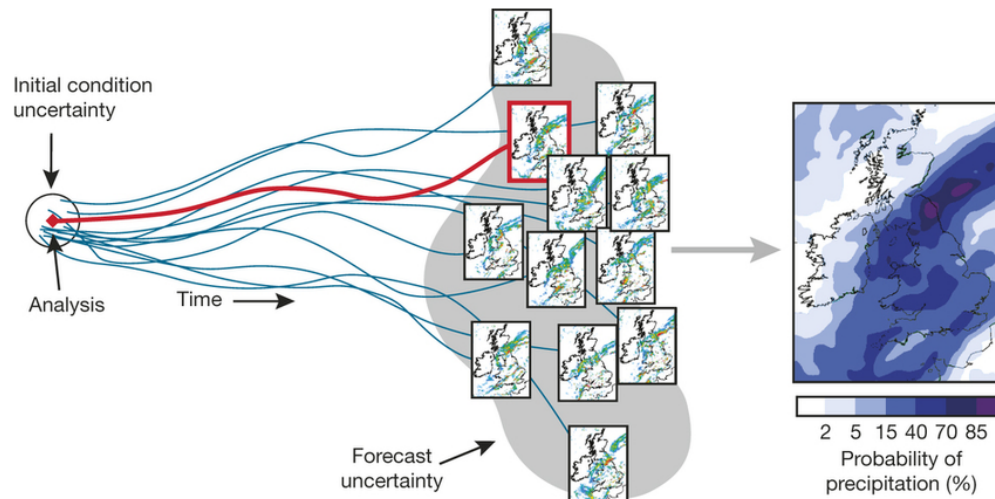
Figure 1: Principle of Ensemble Prediction. Different NWP forecasts are issued from slightly perturbed initial conditions. The resulting ensemble of forecasts samples the distribution of the future atmospheric states.

Different EPSs have been developed by several National Weather Services worldwide. At Météo-France, two EPS are used for operational forecasting, the Arpège-EPS and the Arome-EPS. The Arpège-EPS is based on the global Arpège NWP model and provides forecasts up to 96 hours. Each member of Arpège-EPS starts from different initial conditions, designed with state-of-the-art methods including Singular Vectors (SV) and Ensemble Data Assimilation (EDA). In order to account for the uncertainty of subgrid scale processes each member uses a different package of physical parametrizations (Descamps et al., 2015). The Arome-EPS is based on the regional high-resolution Arome model, that runs over a Western Europe domain centred over France, and provides forecasts up to 51h. For each Arome member, perturbed initial conditions are derived from a specific Arome EDA, lateral boundary conditions are provided by a selected Arpège-EPS member, and the model uncertainty is represented with stochastic perturbations of physics tendencies (Bouttier et al., 2016). The characteristics of the operational Arpège-EPS and Arome-EPS are detailed in the table of Figure 2.

For the purpose of the Smart4RES project, enhanced configurations of Arpège-EPS and Arome-EPS have been developed to improve the prediction of RES variables. These enhanced configurations include a significant increase of the model horizontal resolutions : from 7.5 km to 5 km for Arpège-EPS and from 2.5 km to 1.3 km for Arome-EPS. Resolution increase is obtained with a refinement of the model discretization grid, while the dynamical and physical settings of the models remain the same as for the operational versions. In addition, the frequency of forecast outputs is strongly increased : from hourly outputs to 4-minute outputs (Arpège) and 5-minute outputs (Arome). The size of the Arome-EPS is also increased from 16 to 25 members. The 9 additional members are designed following the same procedure as the 16 members of the operational Arome-EPS. The 25 members are independent and identically distributed.

In order to meet the users needs, the relevant output weather variables and time periods to produce have been defined with Smart4RES partners. Ensemble forecasts are made available to the project over four months : October 2018, August 2019, and February-March 2020. Only the 2019 and 2020 periods are considered in this document.

Arome-EPS	Oper	Smart	**Arpège-EPS**	Oper	Smart
Resolution	2.5km	1.3km		7.5km	5km
Output	1h	5min		1h	4min
Size	16mb	25mb		35mb	35mb
Lead time	51h	51h		96h	96h
LBCs	Arpège oper	Arpège Smart			

Figure 2: Characteristics of Arome-EPS and Arpège-EPS for the currently operational configuration (Oper) and for the Smart4RES high-resolution configuration (Smart). In the next sections the Smart4RES configurations are simply denoted "high resolution ensemble forecasts".

Compared to EPSs currently used in operations the high-resolution configurations developed for Smart4RES are disruptive and correspond to the forthcoming generation of ensemble forecasts that will be available to RES partners in the next 5 years.

The added value of enhanced spatial resolution for ensemble forecasting has been documented in several studies for surface weather variables (Raynaud and Bouttier 2017, Hagelin et al. 2017, Schwartz and Sobash 2017), but its relevance for RES purposes remains to be explored. On the other hand, the value of very high temporal resolution for ensemble forecasting has not yet been adressed in the literature.

In the remainder of this section the impact of the spatio-temporal resolution increases of Arome-EPS is presented for two variables of interest for RES applications : 100-meter wind speed and global horizontal irradiance (GHI).

1.2 Impact of increasing the horizontal resolution

In this section the value of increasing the Arome-EPS resolution from 2.5 km to 1.3 km is assessed. In order to focus on the spatial resolution increase only, the operational and high-resolution ensembles are both used with the baseline output frequency of one hour.

Visual examination

To better understand the differences between 2.5 km and 1.3 km simulations, Figure 3 presents Arome-EPS forecasts of 100-meter wind speed for a specific date of winter 2020, on a subpart of the Arome domain. The high-resolution forecast locally provides slightly larger wind speed values and, as expected, it has a finer representation of orography.
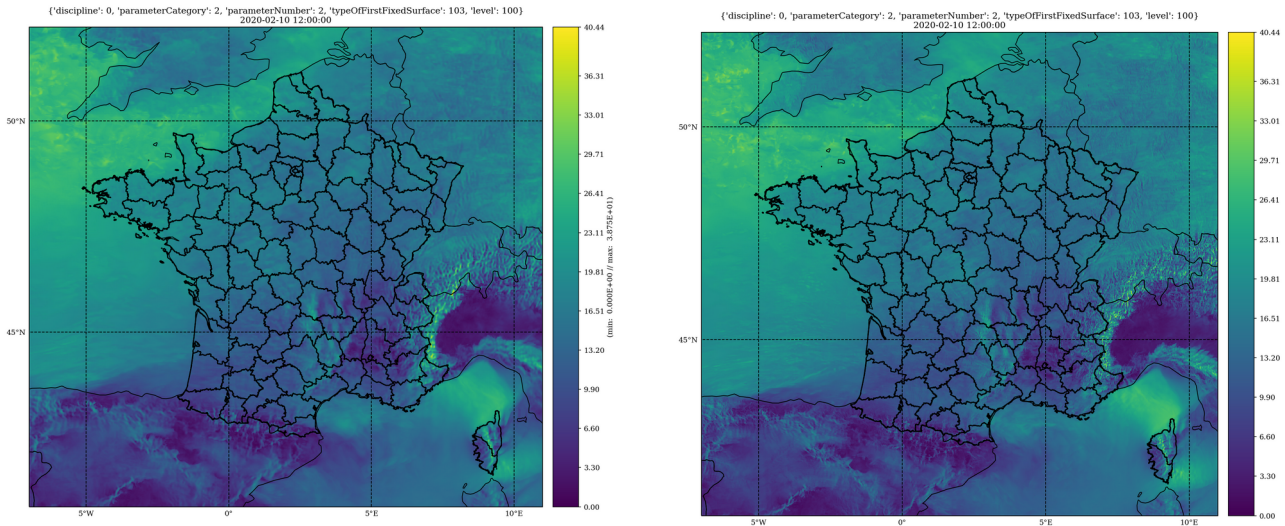
Figure 3: 100-meter wind speed forecast (percentile 90) valid on 10 February 2020 at 12 UTC. (left) Operational Arome-EPS (right) high-resolution Arome-EPS. Unit : m/s.

Evaluation metrics

In addition to visual inspection, the impact of horizontal resolution is measured by computing standard performance scores applied to probabilistic forecasts (Wilks 1995), including :

- the *spread/skill ratio*, a measure of the dispersion of ensemble forecasts. Spread corresponds to the standard deviation of ensemble members, while skill is the root-mean-square error of the ensemble mean. A properly-dispersed ensemble has a spread/skill ratio of 1, while an under-dispersed (resp. over-dispersed) ensemble has a spread/skill ratio below (resp. above) 1.

- the *Receiver Operating Characteristic (ROC) curve*, that represents the True Positive Rate (TPR) as a function of the False Positive Rate (FPR) of a binary event, obtained when varying the decision threshold P_{th}. The TPR and FPR are defined as follows :

$$TPR = \frac{TP}{(TP+FN)} \text{ and } FPR = \frac{FP}{(FP+TN)}$$

with TP the true positives (i.e forecasted event is observed) ; FN the false negatives (i.e observed event is not forecasted) ; FP the false positives (i.e forecasted event is not observed) ; TN the true negatives (i.e event is neither observed nor forecasted). A good forecast has a ROC curve close to the upper left corner (i.e. a high detection rate with a low false alarm rate).

- the *Continuous Ranked Probability Score (CRPS)*, that measures the distance between observation and forecast distributions. Let $F = P[X \leq x]$ be the cumulative distribution function associated with an ensemble forecast X and $F_0 = 1_{[X \leq x_0]}$ be the distribution function associated with the reference observation x_0 (which is then a step function), the CRPS is defined by :

$$CRPS(F, F_0) = \int_R (F - F_0)^2 \, dx$$

The lower the CRPS the better the forecast.

Evaluation of 100-meter wind speed forecasts

Dataset

At the time the evaluation was done (early 2021), the large observations dataset provided by the Smart4RES project partners was not available. As a consequence a reduced dataset of only 21 stations across Europe has been used (Figure 4). These measurements were provided by meteorological masts from the Integrated Carbon Observation System (ICOS, see References), LiDAR data from the SOFOG3D measurement campaign in Southwestern France (see References), and SoDAR data from another network in France that can not be described for reasons of confidentiality. An assessment of the quality of these measurements was performed to ensure the reliability of the reference chosen for the evaluation of the forecasts. As a result, five stations were blacklisted and not included in the computations of the scores "on all stations".

The measurements were available at various heights between 10 and 200 meters: they were therefore vertically interpolated, using a locally adjusted multiplying factor, to match the closest model level (10, 50, 75 or 100 meters, although only the results at 100 meters are presented here since they were the main focus of the study).

The Arome-EPS forecasts used were extracted at the nearest grid point from each station. To properly compare operational and high-resolution forecasts, outputs are extracted from a common grid with a 2,5 km resolution and at a hourly time-step.

Figure 4: Locations of the ICOS and Southwestern France measurement stations used for the evaluation of 100-meter wind speed.

Results

Figure 5 presents the ROC curves for operational and high-resolution Arome-EPS forecasts, computed over February 2020. One can notice that for the three events considered (wind speed above 20 km/h, 30 km/h and 40 km/h), the high-resolution EPS is slightly better than the operational one. This improvement is even more visible in March 2020, but no significant improvement in ROC scores was found in August 2019, as shown in Figure 6 for the 20 km/h threshold for instance. In addition, the dispersion is increased for the high-resolution ensemble at almost all forecast ranges (Figures 7 and 8-left), but the ensemble remains under-dispersive. More work would be needed on the model physics package and the representation of model uncertainty to fix this under-dispersion. Finally, the CRPS, which provides a global measure of forecast performance, also indicates an improvement coming from the high resolution throughout the forecast period (Figures 7 and 8-right), reaching maximum values around 3%. The reliability of the forecasts was also examined with reliability diagrams (not shown here), that assess the agreement between forecasted probabilities and observed probabilities for specific events. They showed a slight degradation for the high-resolution version compared to the operational version, which is directly linked to the increase in the number of members.
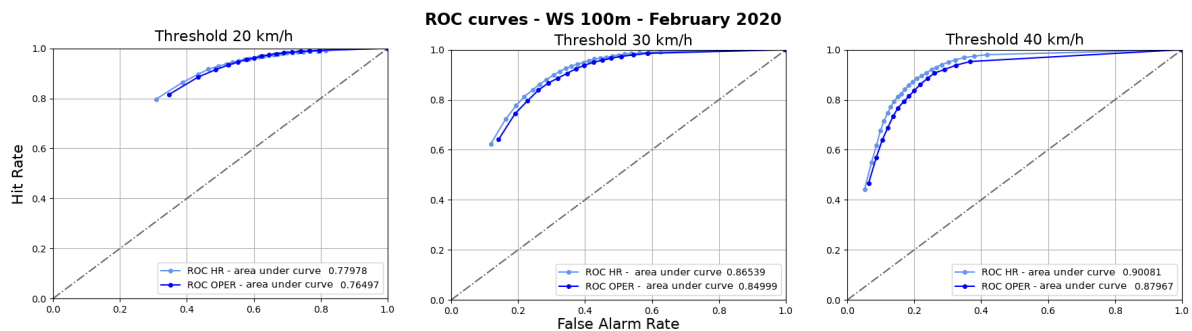
Figure 5: ROC curves for operational (dark blue) and high-resolution (light) Arome-EPS computed over February 2020. Three events are considered : wind above 20km/h (left), 30km/h (middle) and 40km/h (right). Each point on the curve represent the hit rate and false alarm rate for a given probability decision threshold (from 0 to 1).
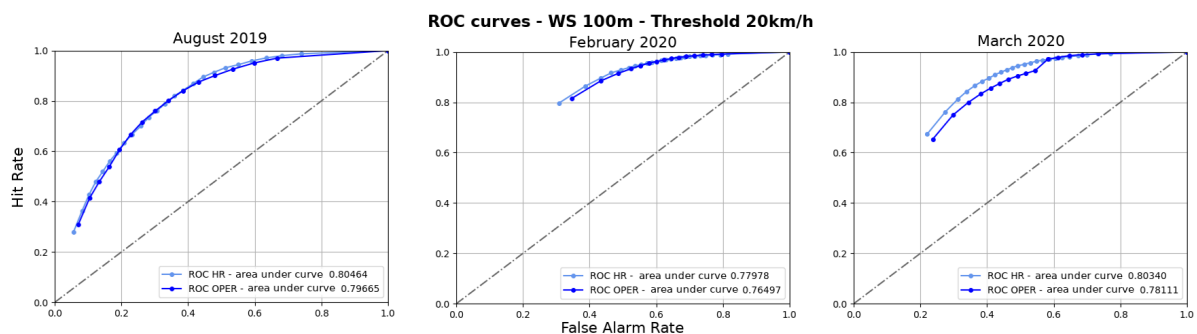
Figure 6: ROC curves for operational (dark blue) and high-resolution (light) Arome-EPS, for the event "wind
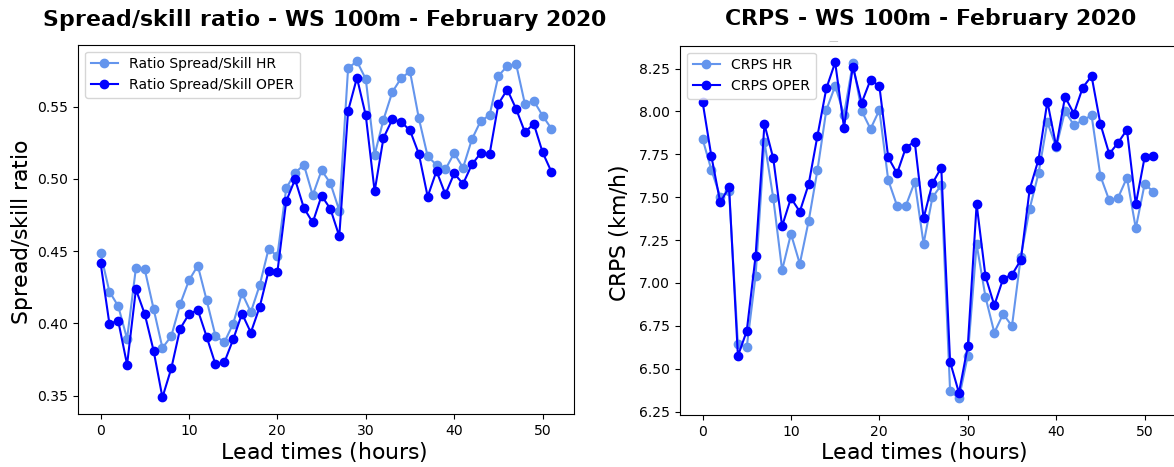
Figure 7: Left : spread/skill ratio as a function of forecast range for operational (dark blue) and high-resolution (light blue) Arome-EPS, computed for February 2020. Right : same for CRPS.
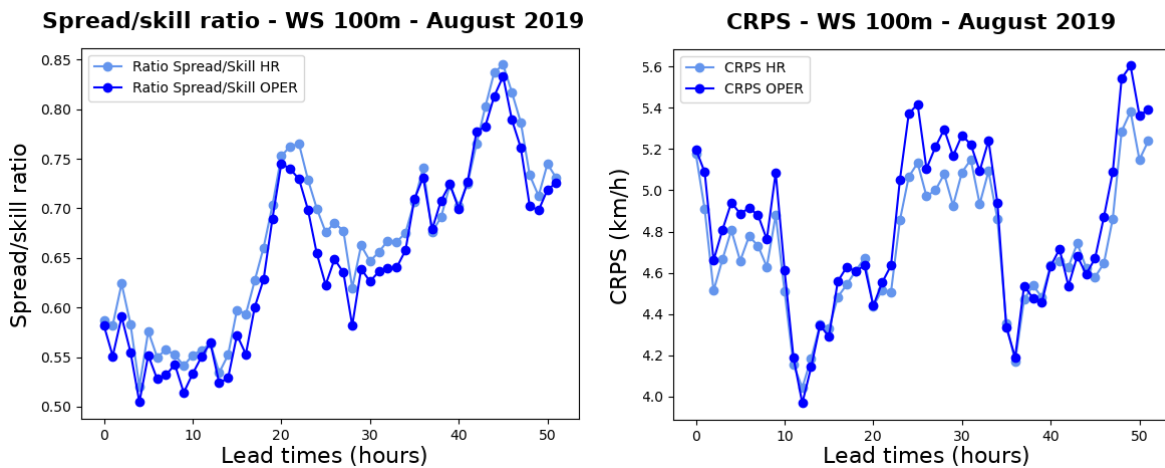
Figure 8: Same as Figure 7 for August 2019.

Evaluation of global solar irradiance forecasts

Dataset

In this part, observations used for the evaluation come from the ground stations equipped with pyranometers from the Météo-France RADOME network (Figure 9, 223 stations are used). Since the quality of these observations is already regularly monitored by Météo-France's meteorological observations department, all stations were considered reliable enough to be used for this study.

The forecasts were extracted the same way as for the 100-meter wind speed evaluation: nearest grid point, 2.5 km resolution and hourly outputs.
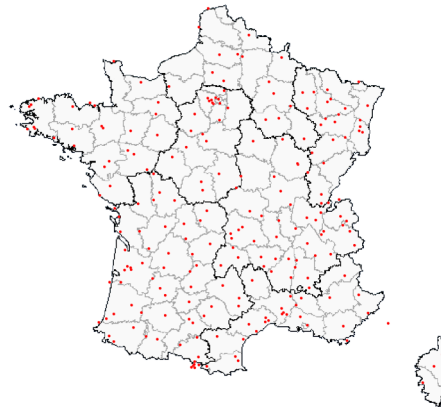
Figure 9: Locations of the GHI measurements used for the evaluation of Arome-EPS.

Results

Figure 10 (left) presents the spread/skill ratio for both operational and high-resolution Arome-EPS. Scores are naturally non-zero only at daytime, and a small increase in spread is obtained with the high-resolution system (but the ensemble remains under-dispersive). The ROC curve in Figure 10 (right) also indicates a small improvement with the increased resolution. An improvement in CRPS is also noticeable in Figure 11, especially in August 2019 for days 1 and 2. Figure 12 summarizes the CRPS improvement coming from the high-resolution for the three months, an average value of ~ 4% is obtained, with a peak around 10% at the end of day 1 (mainly due to the months of August 2019 and March 2020).
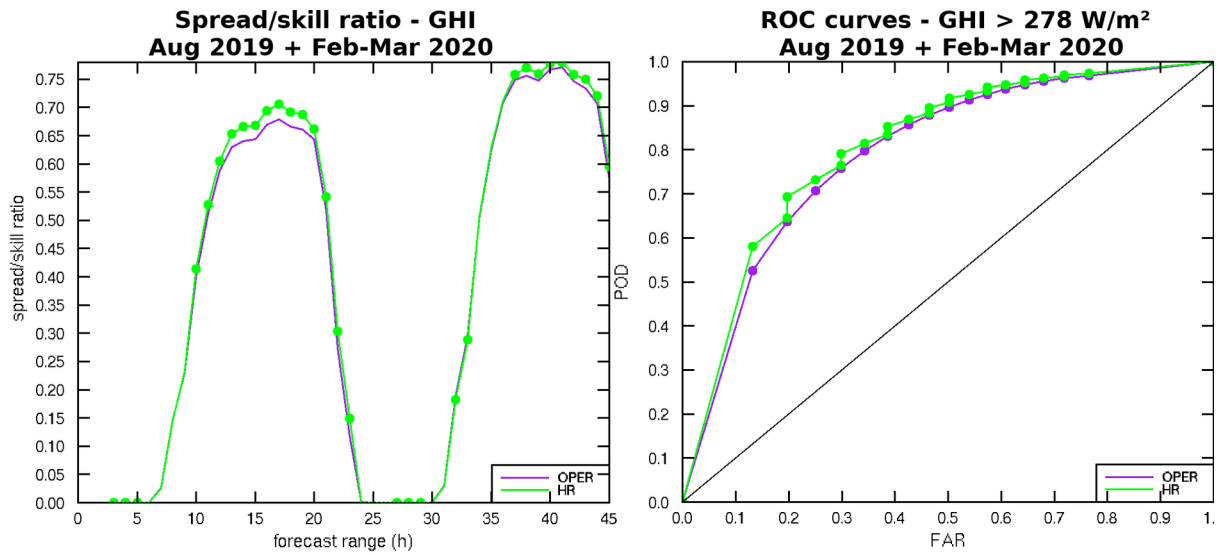
Figure 10: Left : Spread/skill ratio for operational (purple) and high-resolution (green) Arome-EPS as a function of forecast range. This score is computed over a 3-month period (including August 2019, February and March 2020). Right : ROC curve for operational and high-resolution Arome-EPS computed over February 2020).
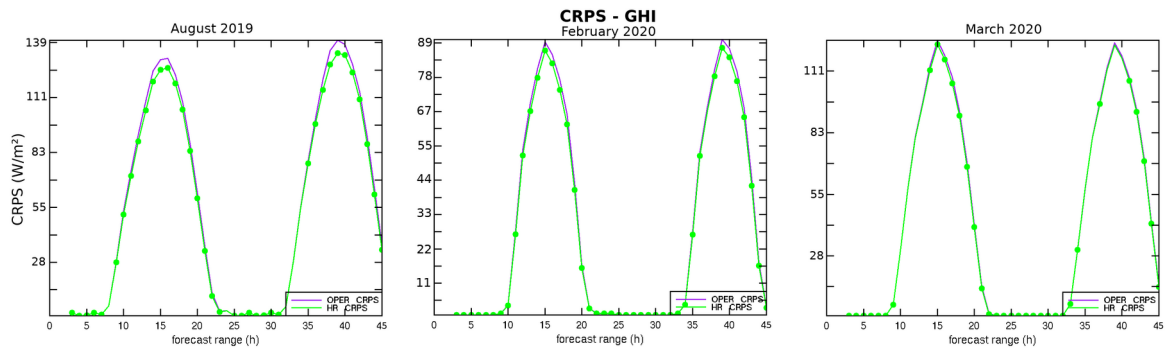
Figure 11: CRPS of global solar irradiance for operational (purple) and high-resolution (green) Arome-EPS as a function of forecast range, computed over August 2019 (left), February 2020 (middle) and March 2020 (right).
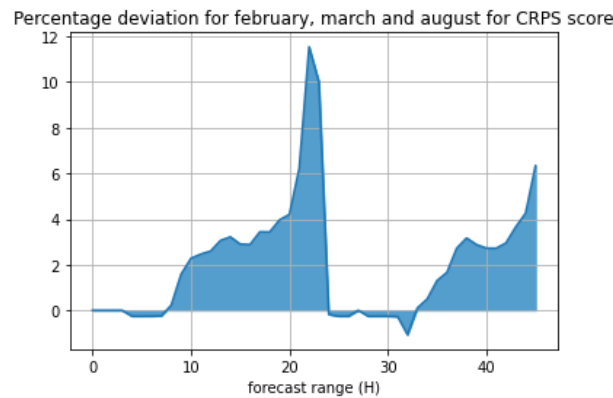
Figure 12: CRPS change obtained with the high-resolution Arome-EPS as a function of forecast range. Positive values indicate an improvement compared to the operational Arome-EPS.

Discussion

The results presented in this section indicate that an increase of horizontal resolution of the Arome-EPS from 2.5 km to 1.3 km provides a consistent ensemble performance improvement around 3-4% on average for the two variables considered, and across the three metrics evaluated. This improvement is almost in line with the KPI 1.1 of the project "*absolute improvement of high-resolution Arome-EPS from few hours up to hundred hours-ahead : 4-6% CRPS for radiative variables; 5-10% CRPS for wind variables*".

This study could be extended to improve the robustness of the results and their statistical significance (not assessed in the present study). For wind speed it would be useful to increase the observation dataset, using for instance the VESTAS measurements that are now available to the project partners. Regarding global horizontal irradiance other types of measurements could also be considered, such as satellite products or pyranometers installed at solar farms.

It is also worth mentioning that increasing spatial resolution is not the only way of improving forecasts. Other NWP refinements are currently under development and evaluation to further improve forecasts performances. At short-term, Arome-EPS will benefit from a new radiative scheme (ecRad, Hogan et al., 2018) and from a new model error representation scheme based on the perturbation of uncertain Arome physics parameters (Wimmer et al. 2021), which is likely to improve the performance of both wind and GHI forecasts. First results from the PhD work of Meryl Wimmer indicate that this new model error scheme allows for an improvement of 10-meter wind speed dispersion and CRPS by 35% and 7% respectively, and for an improvement around 15% for GHI.

Another way to improve forecast performances is by applying a statistical post-processing (Hämäläinen et al. 2020; Schulz et al 2021; Worsnop et al. 2018). However, the training of such methods requires larger datasets of forecast/observation pairs than those available in Smart4RES (only four months).

Finally, one limitation of the current evaluation is that it does not disentangle the impacts of the resolution increase from those of the ensemble size increase. It is thus likely that part of the improvement obtained is due to the increase of Arome-EPS from 16 to 25 forecasts.

1.3 Evaluation of high-frequency forecasts

In this section we assess the ability of the high-resolution Arome-EPS to represent realistic high-frequency variations (5 minutes), for both 100-meter wind speed and global horizontal irradiance. The added value of 5-minute ouputs (compared to hourly outputs) is also examined for the prediction of wind ramp events, which are particularly relevant for wind energy production.

Data and metrics

Dataset

The dataset used for this evaluation consists of :
- 100-meter wind speed measurements from anemometers installed on the nacelles of 121 VESTAS wind turbines with hub heights between 95 m and 105 m (Figure 13a),
- Global horizontal irradiance measurements from pyranometers installed at 72 meteorological stations of Météo-France's observational network (Figure 13b),
- The 100-meter wind speed and global horizontal irradiance from the the high-resolution Arome-EPS, taken at the nearest gridpoints to the observations locations.

Evaluation of the high-frequency forecasts is performed over periods spanning from the 01/08/2019 to the 31/08/2019 and from the 02/02/2020 to the 16/03/2020, hereafter denoted Summer 2019 and Winter 2020 respectively. Figure 14 summarizes the dataset used in the study.
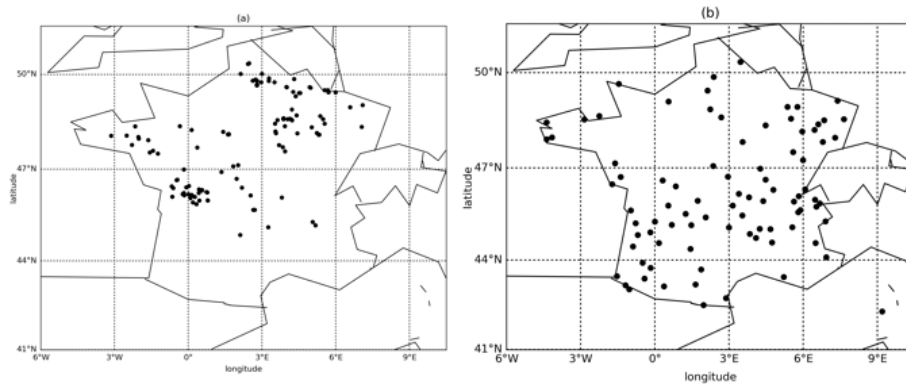
Figure 13: (a) Locations of wind turbines at level around 100m from which wind speed observations are available. (b) Locations of meteorological stations from which global horizontal irradiance are available.

As the observations and ensemble forecasts do not have the same frequency (see table in Figure 14) we apply the following pre-processing :

- Observations of GHI are linearly interpolated in time to obtain values every 5 minutes.

- For 100-meter wind speed, we use forecasts every 10 minutes to be consistent with the observations frequency.

	Observations		High-Res Arome-EPS
	Wind	**PV**	
Variable	Between 95 and 105m wind speed	Irradiance	100m wind speed, Irradiance
Locations	121 wind turbines From VESTAS dataset	72 meteorological Stations in France	Closest gridpoints To observations
Nature	Anemometers on wind turbines Nacelle	Pyranometers	NWP outputs
Periods	Summer 2019 & Winter 2020		
Frequency	10min	6min	5min

Figure 14: Summary of dataset for high-frequency evaluation.

Evaluation methods

In the remainder of this section, we denote N the size of the ensemble, and t the forecast horizon. x and y respectively correspond to observations and forecasts. Recall that a forecast is issued every day at 21:00 UTC, with a maximum horizon T of +48h, and a timestep δ_t of 5 minutes.

High-frequency and low-frequency signals

In order to assess the representation of the high frequency signal of the variables considered in the ensemble forecasts, each variable is decomposed into a low frequency signal (LF) and a high-frequency signal (HF) (Ren et al, 2018). For this purpose, we apply a 1-hour rolling mean filter centred around t to the observations and to each member in the ensemble to obtain :

$$x_t = \overline{x_t} + \epsilon_t^x \text{ and } y_t = \overline{y_t} + \epsilon_t^y$$

With $\overline{x}$ and $\overline{y}$ the LF signal of x and y; and with ϵ^x and ϵ^y the residuals, i.e the HF signal of x and y.

Evaluating the HF signal with standard metrics such as RMSE or bias at every time step is not appropriate since the predictability of this signal is likely to be low. Indeed, km-scale NWP models are not intended to accurately represent temporal variations at the minute scale, however they can provide a useful indication on the range of high-frequency variations over a given time-window. Hence, we adopted a statistical approach to evaluate the ability of Arome-EPS to represent the amplitude and temporal structure of the HF signal, using the following two diagnostics :

- Probability density function (PDF) of observed and forecasted HF signals

The comparison of observed and forecasted PDFs allows to assess the ability of the forecasts to reproduce the amplitude of the HF (and LF) signal.

- Autocorrelation function of observed and forecasted HF signals

The comparison of observed and forecasted autocorrelations allows to assess the ability of the forecasts to reproduce the time structure of the HF (and LF) signal. For instance, we expect the autocorrelation of the HF signal to decay rapidly with the time lag.

Detection of wind ramp events

For wind speed, the quality of high-frequency forecasts is also assessed through their ability to properly detect wind ramps. Ramping events are defined by a large and sudden change in production due to abrupt variations of the resource (and/or cut-out exceeding), and their prediction is very important for RES applications. This study is limited to the wind speed variations, and thus does not address non linearities induced by transformation from wind to power. However, it highlights the added value of using 5 minutes outputs rather than hourly outputs for detecting this kind of event.

Several ways to define and detect ramping events exist in the literature. We use the so-called "fixed time interval" method for ramp detection (Bianco et al. 2016). This simple method is based on the derivative of the wind speed over a given time window $\left(t, t+\delta_t, t+\Delta_t \right)$, to measure the increase or decrease of the wind speed :

$$S(t) = y(t + \Delta_t) - y(t)$$

The function S is then tested regarding a threshold S_0 to decide whether a positive or negative ramp event occurs or not. We define the two timeseries I^+ and I^- of positive and negative ramps occurrence, respectively :

$$I^+_{t:t+\Delta_t} = \begin{cases} 1 \ \text{if} \ S(t) \geqslant S_0 \\ 0 \ \ elsewhere \end{cases}$$

$$I^-_{t:t+\Delta_t} = \begin{cases} 1 \ \text{if} \ S(t) \leqslant -S_0 \\ 0 \ \ elsewhere \end{cases}$$

Note that if I_t is filled by a 1 at an iteration step, the value 1 can not be changed afterward. A schematic example of filling I^+ is shown in Figure 15. In a first step, we apply this detection method to the observed wind speed and to each member of the ensemble. In a second step, we compute the proportion of members forecasting a ramp at any leadtime of the forecast, to obtain a probability of ramp at each timestep of the forecast. For instance, for positive ramps the probability is given by :

$$P_t(ramp+) = \frac{1}{N} \sum I^+_{t,m}$$
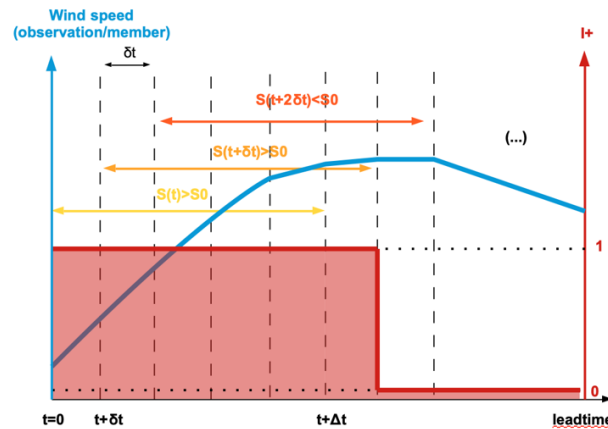
Figure 15: Schematic example of the filling of I+. The blue curve represents the wind speed (y-axis on the left), and the red line represents I+ (y-axis on the right). At the first iteration (in yellow), a ramp is found, so that I+ is filled by 1 over t:Δt ; at the second iteration, a ramp is still found, so that a 1 is added at timestep t+Δt+δt ; at the third iteration, no ramp is found : I+ is set to 0 for timestep t+Δt+2δt.

In a third step, we compute the timeseries I^+ and I^- for the ensemble itself by comparing $P_t(ramp+)$ and $P_t(ramp-)$ to a threshold P_{th}. A common tool to evaluate the ability of the forecast to predict such binary event is the ROC curve, as defined in section 1.2.

Evaluation of 100-m wind forecasts

Figure 16 displays the distributions of the observed and forecasted LF (top) and HF (bottom) wind speed computed using all forecasting dates, locations and leadtimes. The LF wind speed is slightly overestimated by the ensemble over both Summer 2019 and Winter 2020 (Figure 16-(a,b)). The LF wind speed is stronger in Winter than in Summer, with larger extreme values linked to the occurrence of mid-latitude storms. Regarding the HF signal, Figures 16(c)-(d) indicate that the model reproduces the observed distribution quite well for both summer and winter, although large values are slightly under-estimated for both seasons.

Figure 16: Distribution of observed (blue) and forecasted (red) LF wind speed (a) for Summer 2019, (b) for Winter 2020 ; and of HF wind speed (c) for Summer 2019, (d) for Winter 2020.

Figure 17 displays the autocorrelation functions of the observed (blue) and forecasted (red) LF (top) and HF (bottom) wind speed, computed using all forecasting dates, locations and leadtimes. As expected, the autocorrelation of the HF wind speed reaches zeros rapidly after about 30 minutes. This behaviour is well reproduced by the ensemble forecasts, although the decorrelation time scale is slightly over-estimated. The autocorrelation of the LF wind speed is well reproduced by the ensemble forecast as well.

Figure 17: Autocorrelation of observed (blue) and forecasted (red) LF wind speed (a) for Summer 2019, (b) for Winter 2020 ; and of HF wind speed (c) for Summer 2019, (d) for Winter 2020. The autocorrelation is given for lags from 0 to 3 hours.

In order to evaluate the added value of using high frequency ensemble forecasts for the detection of wind ramps, two ramps forecasts are compared :
- a high-resolution one, using the high-frequency 10-minute ensemble wind forecasts
- a low-resolution one, using only hourly ensemble forecasts and a linear interpolation to the 10-minute frequency

These two forecasts are compared to the observed ramps, computed using the 10 minutes observations. We apply ramp event detection to both ensemble forecasts as described previously, with ramp characteristics set to $\Delta_t = 3h$ and $S_0 = 6\,m/s$. We compute TPR and FPR for each ensemble and for P_{th} varying from 0 to 1, with increment $1/N$ to plot the ROC curve displayed in Figure 18. The figure shows that using high-frequency forecasts leads to a larger detection rate than using lower-frequency forecasts, for both positive and negative ramping events.
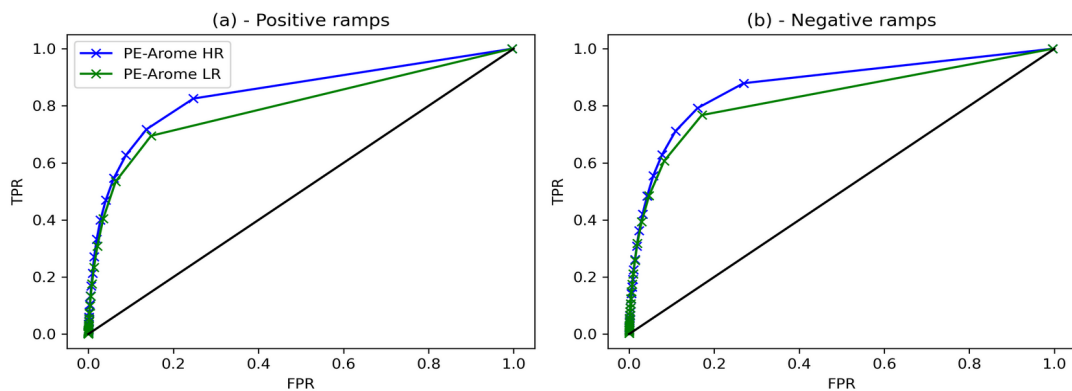
Figure 18: ROC curve obtained from ramping event detection with the high-frequency ensemble forecast (blue) and with lower-frequency ensemble forecast (green) over the Winter 2020 period, (a) for positive ramps, (b) for negative ramps. Each cross on the curves represents the hit rate and false alarm rate for a specific decision threshold (ranging from 0 to 1 with an increment of 1/N).

Evaluation of global horizontal irradiance forecasts

Figure 19 shows the distributions of the observed and forecasted LF (top) and HF (bottom) surface irradiance. Nighttime values have been artificially removed to avoid too high peaks of probability around zero. Both distributions of the LF and HF surface irradiance are well reproduced by the ensemble forecasts.
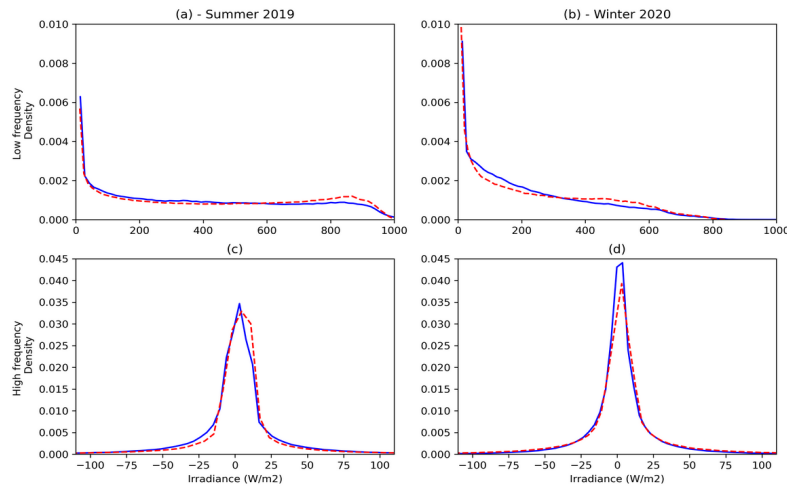
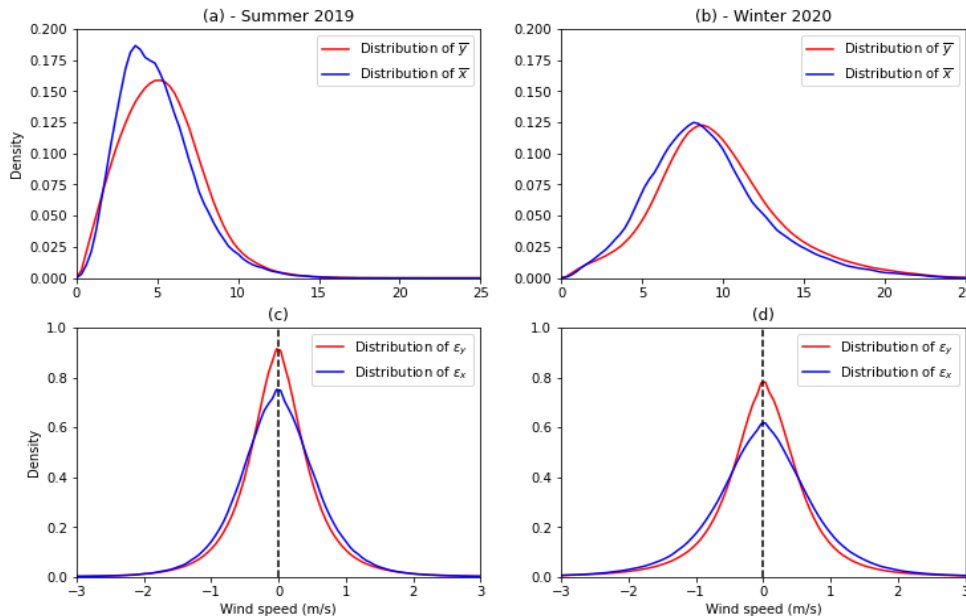*Figure 19: Distribution of observed (blue) and forecasted (red) LF GHI (a) for Summer 2019, (b) for Winter 2020 ; and of HF GHI (c) for Summer 2019, (d) for Winter 2020. Note that nighttime values have been artificially removed to avoid too high peaks of probability around zero.*

Figure 20 displays the autocorrelation functions of the observed (blue) and forecasted (red) LF (top) and HF (bottom) signals. As for the wind speed, the autocorrelation of the HF GHI rapidly reaches zero after less than 1 hour. It becomes negative afterward due to the daily cycle, to finally remain almost null after 1.5 hours. We also note that the decorrelation time scale is slightly under-estimated. The autocorrelation of the LF GHI is well reproduced by the ensemble forecasts, although a small over-estimation.
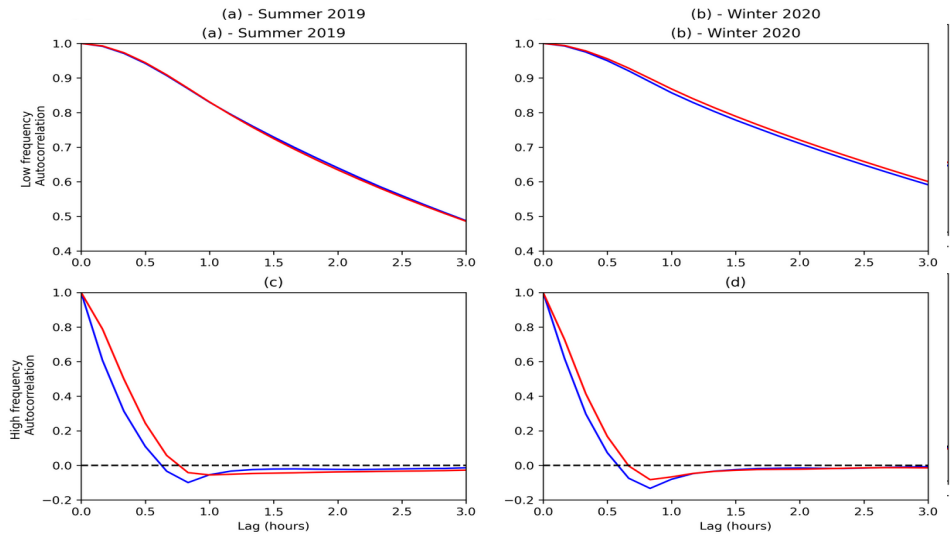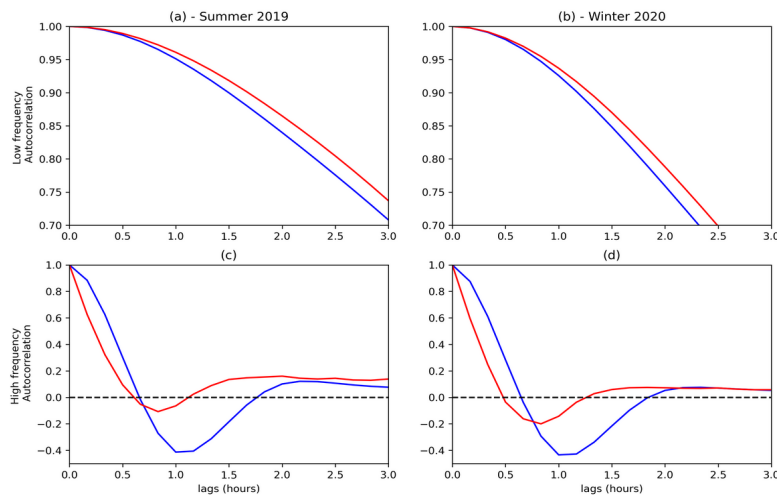

Figure 20: Autocorrelation of observed (blue) and forecasted (red) LF surface irradiance (a) for Summer 2019, (b) for Winter 2020 ; and of HF surface irradiance (c) for Summer 2019, (d) for Winter 2020. The autocorrelation is given for lags from 0 to 3 hours.

Conclusions

The value of high-frequency forecasts from a high-resolution Arome-EPS has been evaluated for the first time in the context of the Smart4RES project.

Using a decomposition of the wind speed and surface irradiance into LF and HF signals, the high resolution ensemble is shown to reproduce the high frequency variability of the two RES-relevant variables quite well. For the wind speed, the high-resolution Arome-EPS slightly under-estimates the amplitude of the HF signal and over-estimates its decorrelation timescale. For the surface irradiance, the amplitude of the HF signal is well predicted and the decorrelation timescale is slightly under-estimated.

In order to perform a user-oriented evaluation, a detection of ramping events has also been developed, following the methodology proposed in previous works. A major result is that high frequency forecasts allow for a higher detection rate of these events than standard hourly outputs.

These results on the high-resolution information content are very promising and could lead to the development of new forecasting products to inform on the high-frequency variability of the wind and solar resources.

Overall, combining high spatial resolution and high-frequency outputs should clearly improve the value and utility of Arome-EPS forecasts for RES purpose.

2. High-resolution weather forecasting for renewables with Large-Eddy Simulations

Large-eddy simulation is traditionally used in academic settings, for example to study NWP cloud or turbulence parameterizations (De Roode S.R., 2012) or wind farm flow physics (Stevens and Meneveau, 2017). Advances in scientific computing have paved the way for using LES in an operation context. Two use cases are particularly relevant for renewable energy: 1) wind or solar resource and annual energy production (AEP) assessments and 2) short-term forecasting.

Based on pioneering work at TU Delft (Schalkwijk et al., 2012, Schalkwijk et al., 2015), Whiffle has further developed an LES model that runs almost entirely on Graphics Processing Units (GPU). This model, abbreviated with GRASP (GPU-Resident Atmospheric Simulation Platform), has been used for operational wind farm forecasts since 2016, using input data from the European Centre for Medium range Weather Forecast (ECMWF) High Resolution (HRES) model. Run-time constraints are dictated by the time between ECMWF forecasts become available. Typically, the operational GRASP forecast models are run on a resolution between 50m-100m, which, on a modern GPU, results in a runtime of less than an hour for a 48h horizon forecast. See Gilbert et al., 2020 for more information about the performance and an offshore wind farm case study.

In this report, we focus on the application of the GRASP LES model in a day-ahead forecasting setting for a number of locations of interest for the Smart4RES project. We give a concise description of selected aspects of the model formulation in section 2.1 and present the case study set-up and results in section 2.2. The results section focusses on a comparison of forecasted meteorological variables with observation data, i.e. the conversion of power forecasts has not been considered in this document.

2.1 Introduction into atmospheric LES

In the following paragraphs, we provide a brief overview of some aspects of LES in the context of forecasting for renewables. LES differs from numerical weather prediction (NWP) mainly in its treatment of turbulence and clouds. The idea behind LES is to resolve the energy carrying part of the turbulent spectrum by solving the filtered Navier-Stokes equations and cloud thermodynamics. In this way, LES does not have to rely on cloud and boundary layer turbulence parameterizations like traditional NWP models.

Governing equations

We present the most important governing equations below. More details can be found in Heus et al., 2010, Böing, 2014 and Schalkwijk et al., 2015. We follow Einstein's summation notation, with $x_1, x_2, x_3 = x, y, z$ for the coordinates and $u_1, u_2, u_3 = u, v, w$ for the wind components. The continuity equation reads:

$$\frac{\partial}{\partial x_j} \rho u_i = 0$$

In the anelastic approximation employed in GRASP, the density $\rho = \rho(z)$ represents a base density profile depending on height only.

$$\rho \frac{\partial u_i}{\partial t} = -\frac{\partial \rho u_i u_j}{\partial x_j} + \frac{\partial \tau_{ij}}{\partial x_j} - \frac{\partial p'}{\partial x_j} + \delta_{i3}\rho B + \varepsilon_{ij3}f(u_j - u_{geo,j}) + \left(\frac{\partial \rho u}{\partial t}\right)_{\text{sources}}$$

In the Navier-Stokes equation above, we denote buoyancy with B. The pressure gradient term has been written as a geostrophic wind u_{geo}. Further, we have the turbulent stress τ_{ij} which needs to be modeled with an appropriate turbulence closure. One of the main challenges in LES modeling is the closure problem: expressing the sub-grid contributions of momentum transport (τ_{ij}) in terms of resolved quantities. There is a wide variety of sub-grid models, of which a significant class use the concept of *eddy viscosity*:

$$\tau_{ij} = -2K_m S_{ij}$$

Where S_{ij} is (symmetric part of) the strain-rate tensor, or, more descriptive in the context of fluid dynamics: the velocity gradient tensor.

$$S_{ij} = \frac{1}{2}\left(\frac{\partial u_i}{\partial x_j} + \frac{\partial u_j}{\partial x_i}\right)$$

GRASP has several options for the eddy viscosity model, the simplest being the well-known Smagorinsky model. Transport of moisture is described by:

$$\rho_b \frac{\partial q_t}{\partial t} = -\frac{\partial \rho_b u_j q_t}{\partial x_j} - \frac{\partial F_j^q}{\partial x_j} + S_{q_t}$$

Where $q_t = q_v + q_l + q_i$ denotes the conserved variable total specific humidity, being the sum of vapor, liquid and ice water. Sub-grid fluxes or humidity are denoted F^q and other sources of of humidity are denoted by S_q.

Transport of heat is described by:

$$\rho_b \frac{\partial \vartheta_l}{\partial t} = -\frac{\partial \rho_b u_j \vartheta_l}{\partial x_j} - \frac{\partial F_j^\vartheta}{\partial x_j} + S_{\vartheta_l}$$

Where we use a temperature:

$$\vartheta_l = \frac{h_l}{c_p} - T_0$$

that is based on moist static energy h_l:

$$h_l = c_p T + gz - L_v q_l - L_i q_i$$

This is a conserved variable for moist adiabatic ascent.

Boundary conditions

Large-scale NWP When coupling the LES to a large-scale model, several terms are adjusted/added:

$$\rho \frac{\partial u_i}{\partial t} = \cdots + \varepsilon_{ij3} f(u_j - u_{geo,j}^{LS}) - \rho u_i^{LS} \frac{\partial u_j^{LS}}{\partial x_j} - w^{LS} \frac{\partial u_i}{\partial z} + \frac{1}{\tau} \left(u_i^{LS} - \overline{u_i} \right)$$

$$\frac{\partial \phi_i}{\partial t} = \cdots - \rho u_i^{LS} \frac{\partial \phi_j^{LS}}{\partial x_j} - w^{LS} \frac{\partial \phi_i}{\partial z} + \frac{1}{\tau} \left(\phi_i^{LS} - \overline{\phi_i} \right)$$

Where φ denotes a conserved scalar variable (temperature or humidity). The terms with superscript *LS* thus have to be diagnosed from the large-scale model. Currently we use ECMWF for that, but in principle other models could be used.
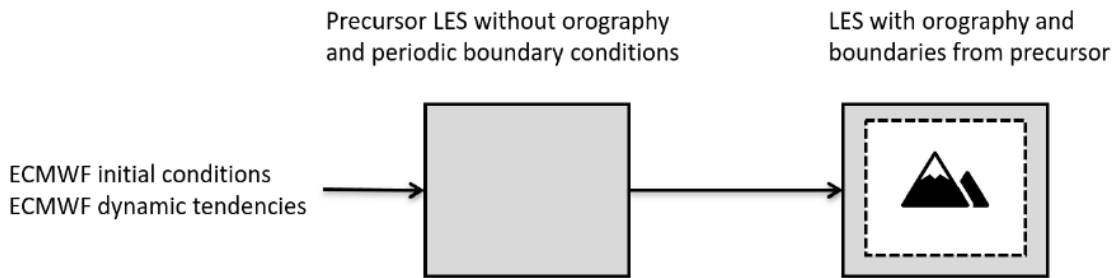
Figure 21: Schematic view of ECMWF boundary conditions, a precursor simulation and a nested domain.

Lower boundary conditions GRASP uses a modified version of the ECMWF TESSEL scheme for its lower boundary condition (ECMWF, 2017; Tiggelen, 2018). In this scheme, the surface fluxes are parameterized using Monin-Obukhov (MO) similarity theory. Obstacles and orography are represented using the immersed boundary conditions method in combination with a displacement height in the MO functions. The representation of soil properties is done by a user defined mapping of a high-resolution land-use dataset (in the case of Europe: the Corine Land Cover data) to the TESSEL soil classes.

Nesting GRASP allows user to nest different simulations during runtime, for example to run a higher resolution LES in a region of interest. Over a user-specified boundary region, the values of the inner nest simulation's variables are nudged towards the parent simulation, also referred to as a precursor simulation. A typical set-up for a simulation with heterogeneous terrain is shown in Figure 21.

Radiation

Radiative transfer calculations are important for the atmospheric heating rates and the surface energy balance. In addition, for solar energy applications, downwelling solar radiation is the most important forecast variable. GRASP radiation can be run in two

modes: 1) off-line, in which the radiation calculations are done based on the hosting NWP atmospheric variables and 2) interactively, in which the GRASP cloud/temperature variables are being used. The off-line mode has the benefits that it is much faster. GRASP uses the ECMWF radiation settings based on RRTMG with the Tegen climatology for aerosols and greenhouse gases (ECMWF, 2017). Currently, an upgrade to ECrad with the CAMS aerosol climatology is being implemented (Hogan & Bozzo, 2018).

Wind turbine parameterization

For wind energy forecasts, the LES model offers the possibility to include windturbines in the simulation using a so-called actuator disk model. This models the turbine as semi-permeable disk that exerts forces on the flow that are consistent with the thrust curve of the wind turbine. In this way, wind farm wake effects are taken into account. In addition, using the turbine power curve, the turbine parameterization allows to directly simulate power output per turbine on a high temporal resolution. Readers are referred to Meyers and Meneveau, 2010, Stevens et al., 2014 and Gilbert et al., 2020 for more details on actuator disk models in LES models of wind farms.

2.2 Case studies

Within the Smart4RES project, a number of case studies focussing on LES based renewable energy forecasts have been performed. They cover both wind and solar energy forecasts over a range of sites. Below we present the set-up and the results of the four case studies. In all cases, a comparison will be made with the ECMWF model, since this is both a useful benchmark forecast in itself, but also the model from which the boundary conditions are derived to drive the LES model. A reasonable requirement for any meso- or micro-scale or model is that it should not deteriorate the forecast skill of the hosting model. Furthermore, the runtime should not be excessive, so that the forecasts can be disseminated quickly after receiving the hosting model data. In an operational setting, GRASP receives the ECMWF data around 07 UTC time and then for most RES related purposes has a maximum of two hours of runtime. For day-ahead trade, the forecasts usually need to be delivered well before 12h local time, which is often the gate closure time of the day-ahead market. The forecast has to cover at least the 24h period starting from 00h local time after the day-ahead market closure to the next 00h local time. Seen from the starting point of the ECMWF data-assimilation cycle, this forecast thus covers a period of +24h to +48h ahead (save the time difference of local time and UTC). Figure 22 shows the timeline of this forecasting process in a schematic way.
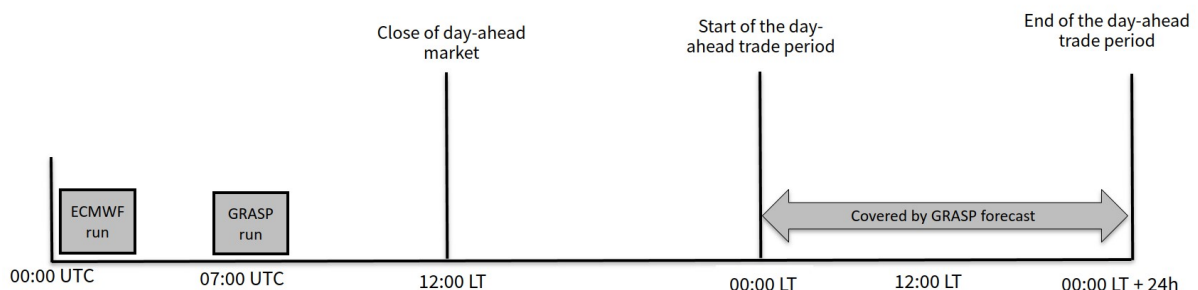
Figure 22: Schematic of forecasting timeline.

Rhodos

The Greek island of Rhodos forms a case study because data of a number of wind farms are available in the Smart4RES consortium. Figure 23 shows the island and the four wind farms. Two are located in relatively mountaineous terrain at a distance of roughly 10 km to the coast. The other two are much closer to the coast in less mountaineous terrain. More detailed orography and land use maps of the four sites are shown in Figures 24, 28 and 30.
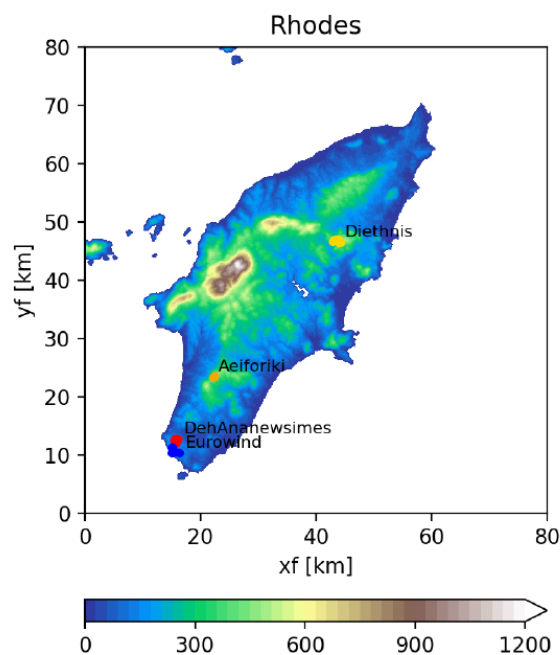
Figure 23: Overview of the terrain height of Rhodes and the locations of the four windfarms.

Aeiforiki The Aeiforiki windfarm is situated in complex terrain conditions, on a pronounced mountain ridge, with up to 600m height differences within an area of 10km x 10km.

Setup The domain size is chosen as 15.4km x 15.4km. Further domain settings can be found in Appendix A. The wind farm situation, surrounding orography and land cover can be seen in Figure 24.

(a) Height map   **(b)** Corine land cover
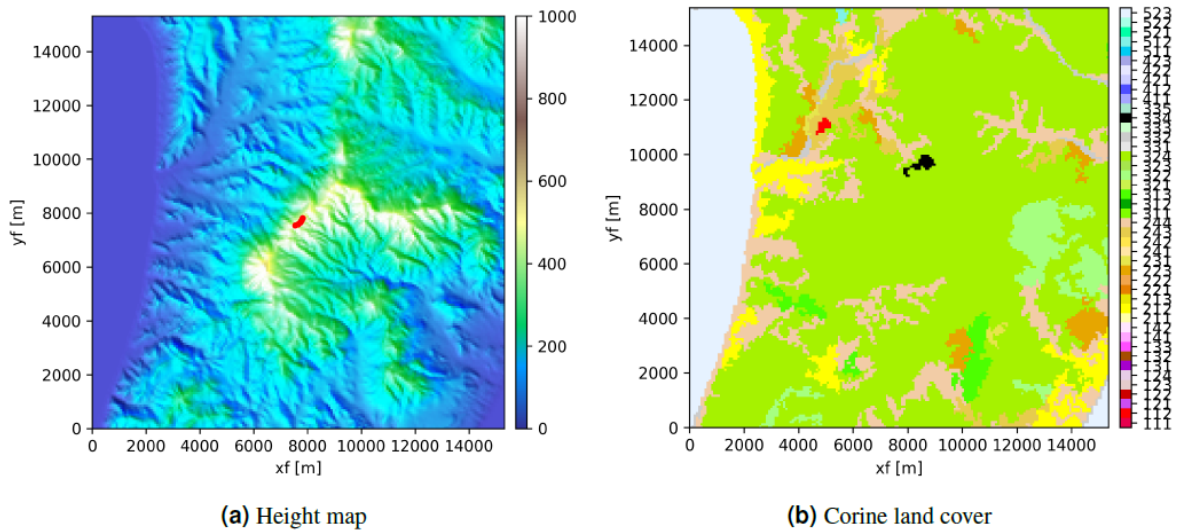
Figure 24: Height map and land use of the Aeiforiki domain.

Results Figure 25 shows scatter plots and error metrics of the Aeiforiki wind farm for both GRASP and ECMWF data. On all error metrics, GRASP forecasts have signicantly better scores. Figure 25a shows that the ECMWF forecast suffers from a particularly large bias (underprediction) of 2.4 m/s or nearly 30% of the observed mean wind speed. This bias weighs heavily in the RMSE and MAE scores, too. In the GRASP forecasts, the bias is almost completely removed: 0.3m/s or 0.37 m/s or 4.5%, which leads to marked improvements in MAE and RMSE. The correlation coefficient and RMSD scores of GRASP are also better, but the difference with ECMWF is less pronounced than for the bias-senstive metrics.

To gain more insight in the observed differences between GRASP and ECMWF, we show wind speed distributions and fitted Weibull parameters in Figure 26. Whereas the mode of the distribution lies around 7.5 m/s for all three datasets, we observe that ECWMF completely lacks wind speeds larger than 15 m/s. GRASP still shows a small underestimation of wind speeds larger than 12.5 m/s, but captures overall the distribution better.

As an illustration, we have plotted hourly mean wind speeds for a randomly selected hour of the dataset: in this case the 3rd hour of the first day of the dataset, i.e. 2018-01-01 03:00h UTC. Figure 27 shows a horizontal wind speed map at 80m above the terrain height and a vertical cross-section (with dimensions x-distance, or east-west distance, and height) of wind speed at a plane at half the domain size. In Figure 27a one can distinguish the terrain features such as the acceleration over the mountain ridges. We recall that a single ECMWF grid-box covers roughly the entire domain shown in Figure 27a, so these terrain details cannot be resolved by the ECMWF model. This partly explains the bias of the ECMWF model. Figure 27b shows the vertical cross-section of wind speed. The acceleration over the ridge is clearly visible and is most pronounced on the west side (right side in the figure) of the domain.

(a) ECMWF vs. SCADA
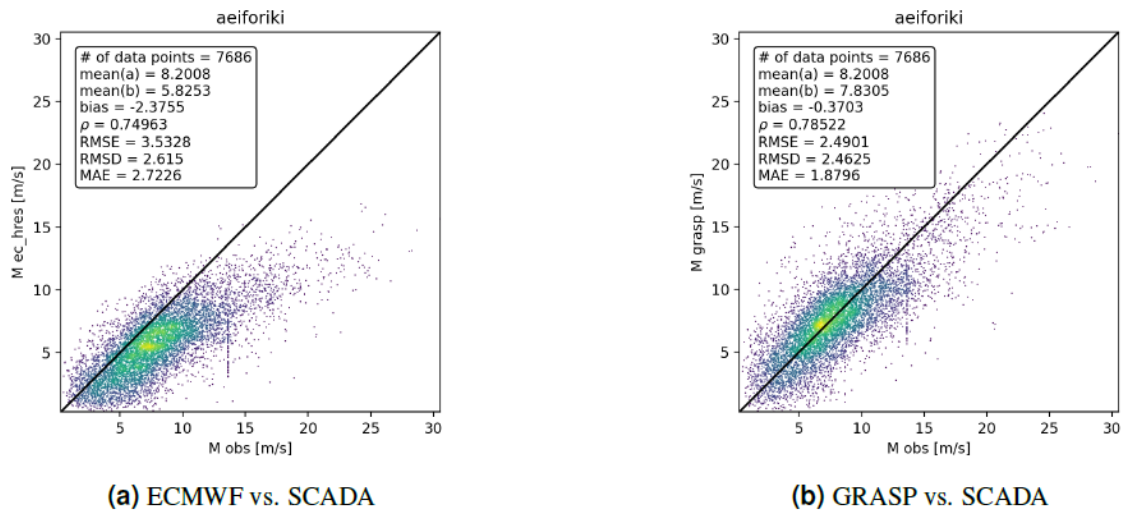
(b) GRASP vs. SCADA

Figure 25: Scatter plots of ECMWF and GRASP vs. SCADA hourly mean wind speeds for the Aeiforiki wind farm.

(a) Observations
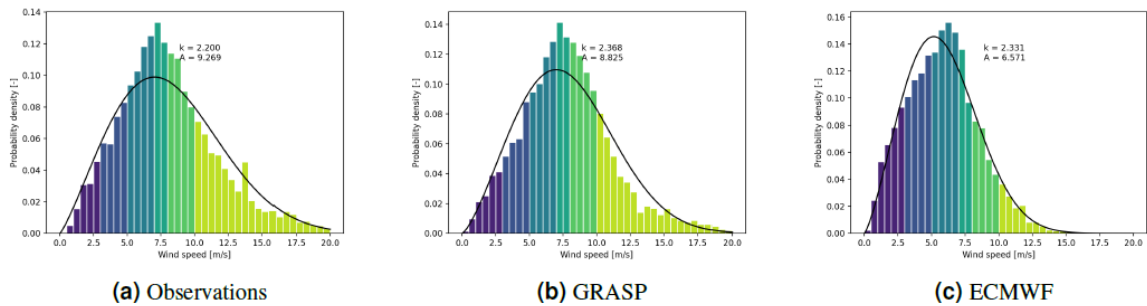
(b) GRASP

(c) ECMWF

Figure 26: Wind speed distributions and fitted Weibull parameters for GRASP, ECMWF and SCADA measurements at the Aeiforiki wind farm.

(a) wind speed 80m above ground

(b) vertical cross-section of wind speed
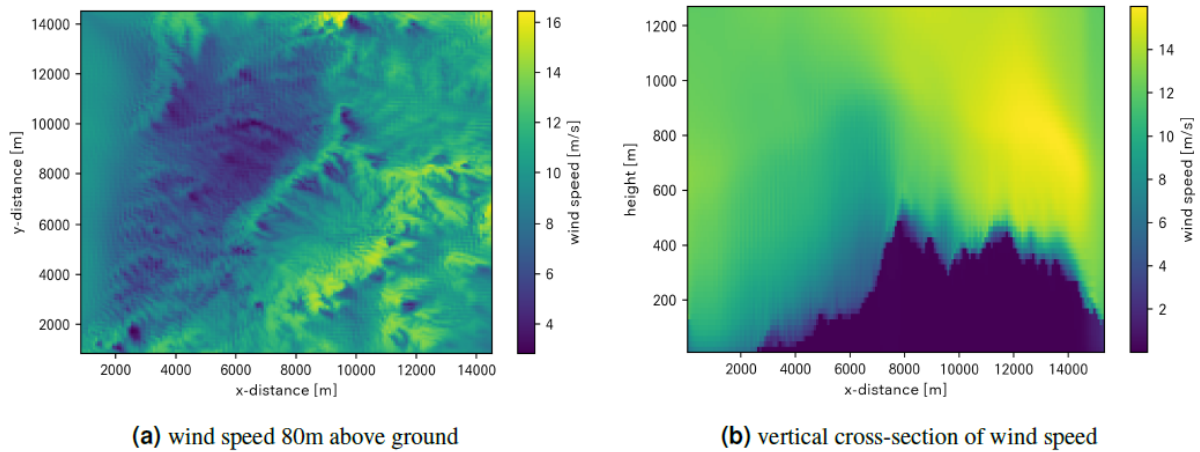
Figure 27: Horizontal and vertical wind speed maps of Aeiforiki wind farm for 2018-01-01 03:00h.

Because GRASP is a turbulence resolving model, its output contains turbulent fluctuations on a high temporal resolution. Figure 28 shows four 48-hour time series of observed and forecasted wind speed for one of the turbines in the Aeiforiki wind farm. The time resolution of all data sources is one minute and the ECMWF hourly values have been linearly interpolated.
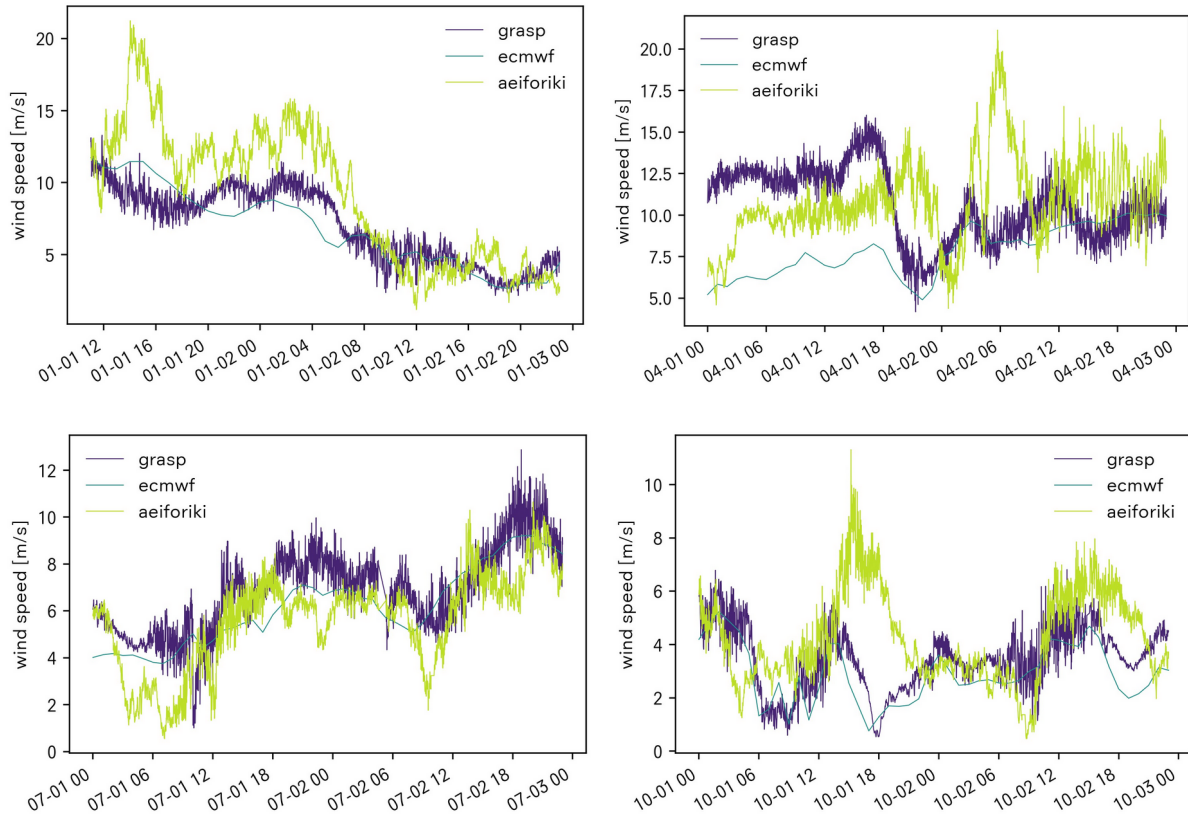
Figure 28: Time series of Aeiforiki SCADA data, GRASP forecasts and ECMWF forecasts for two days in January (top left), April (top right), July (bottom left) and October (bottom right).

Upon visual inspection of the time series, GRASP shows turbulent fluctuations of comparable magnitude than the observed ones. Both GRASP and the SCADA measurements show periods of markedly lower turbulence such as in the night of July 1st between 00h and 06h.

To gain more insight in the ability of GRASP to correctly represent typical wind speed fluctuations, we analysed wind speed ramps over different time intervals. For an averaging period Δt, we define the ramp as the difference in wind speed over two consecutive averaging intervals: $r(t;\Delta t) = \overline{M}(t + \Delta t) - \overline{M}(t)$, where the overline denotes a time average over Δt. Because turbulence is a stochastic process, a point-by-point comparison of forecasted and observed individual ramp events is not meaningful. Instead, we are interested in whether the probability distributions of the forecasted ramps are similar to the observed ones. Therefore, we compute the cumulative distribution functions of the ramps over different averaging intervals.

Figure 29 shows the cumulative distribution functions of ramps of different averaging intervals for GRASP and the observations from Aeiforiki. ECMWF values have been shown for reference, but since they are linearly interpolated values from 1h data, the ECMWF

ramps smaller than one hour should be interpreted with caution. For the fluctuations on 1-minute and 5-minute timescale, GRASP shows a good agreement with the observations. For time-scales of 15 minutes to one hour, GRASP shows less fluctuations than the observations. For the 3-hour time scale, both ECMWF and GRASP are closer to the observations.
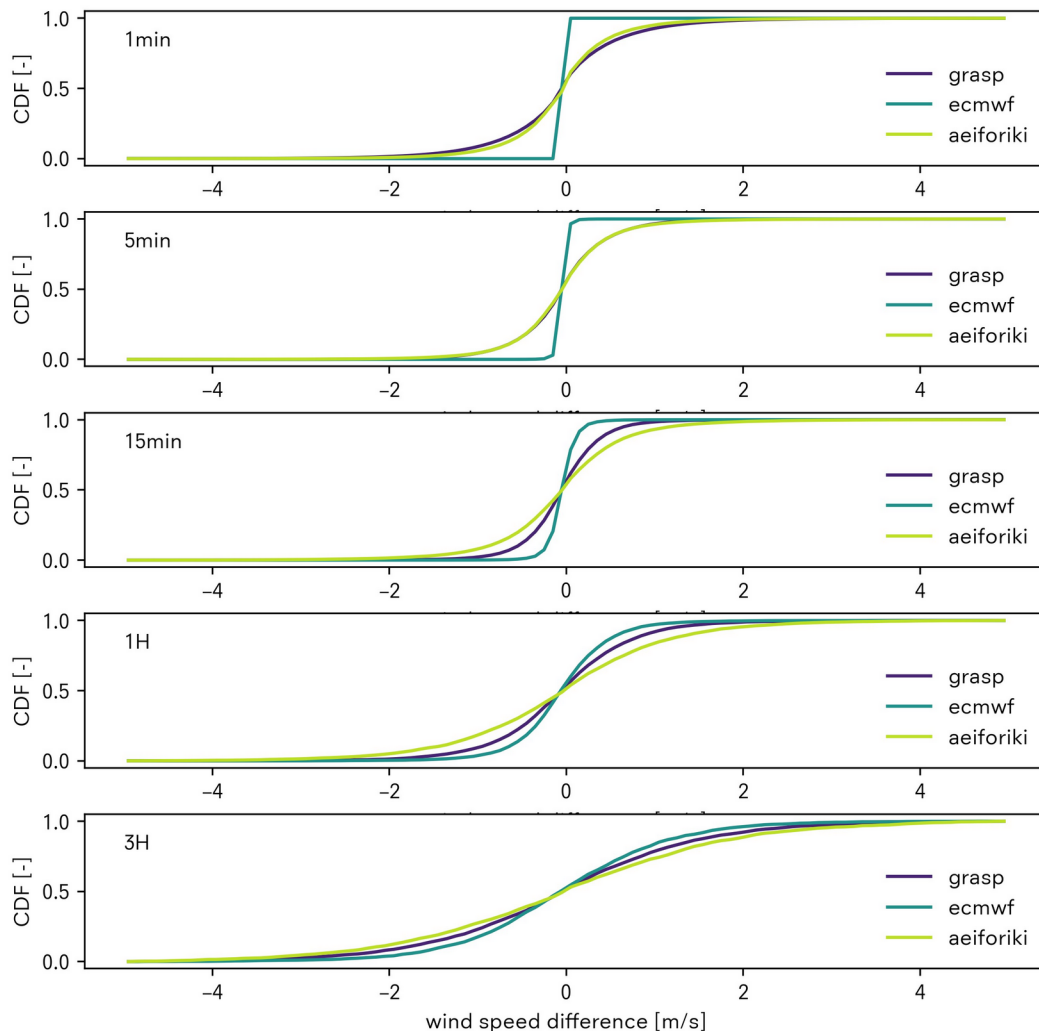
Figure 29: Cumulative distribution functions of wind speed ramps over different averaging intervals.

One hypothesis to explain the too narrow distribution of windspeed fluctuations of 15 minutes to 1 hour is that the current GRASP setup does not fully capture mesoscale fluctuations. Small-scale turbulence is represented well and is circulated through the domain by means of the periodic boundary conditions. Large-scale (1 hour) fluctuations are mostly the result of the applied tendencies from the ECMWF boundary conditions. The extent of the GRASP domain (15km) is too small to generate mesoscale dynamics.

Another instructive metric to compare time series is the autocorrelation function. In Figure 30 we show the autocorrelation for the Aeforiki wind speeds and the two forecasts. The autocorrelation of the GRASP signal first falls rapidly and then more slowly and with roughly the same rate as that of ECMWF. Compared to the observations, the rate of decorrelation in GRASP for the first few minutes is somewhat too strong, but after a lag of

This project has received funding from the European Union's Horizon 2020 research and innovation programme under grant agreement No 864337

35

15 minutes the correlation remains too high. Again, this figure signals that mesoscale dynamics may not be present in GRASP.
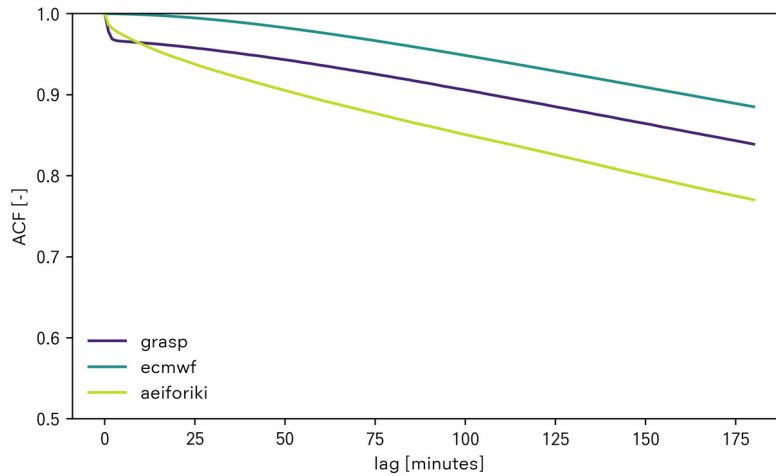
Figure 30: Autocorrelation function up to a lag of 3 hours.

Diethnis Similar to the Aeiforiki windfarm, the Diethnis wind farm site is situated in complex terrain conditions, on a pronounced mountain ridge. Orography and land use in the domain are similar too.

Setup The domain size is chosen as 15.4km x 15.4km. Further domain settings can be found in Appendix A. The wind farm situation, surrounding orography and land cover can be seen in Figure 31.

(a) Height map

(b) Corine land cover
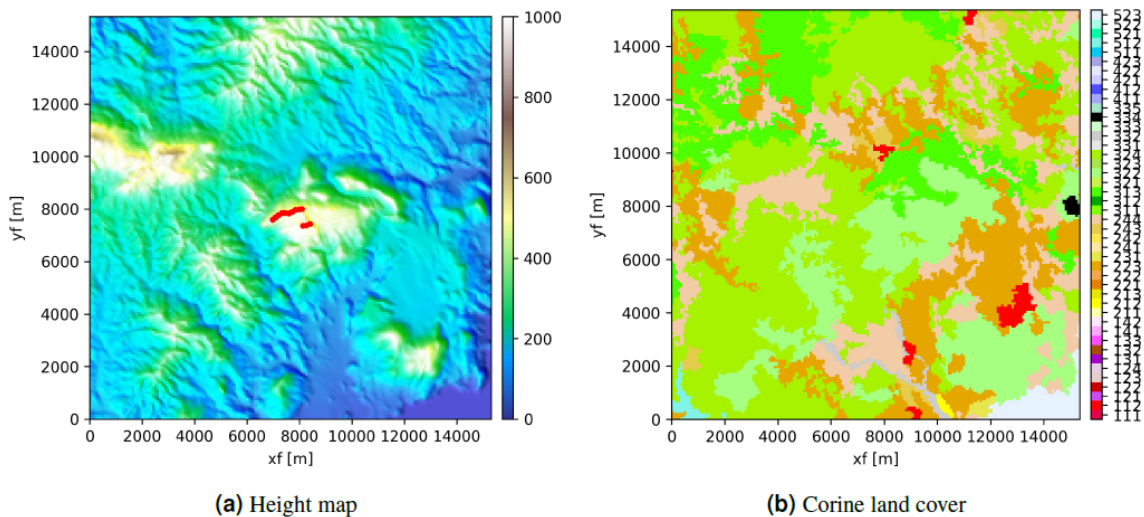
Figure 31: Height map and land use of the Diethnis domain.
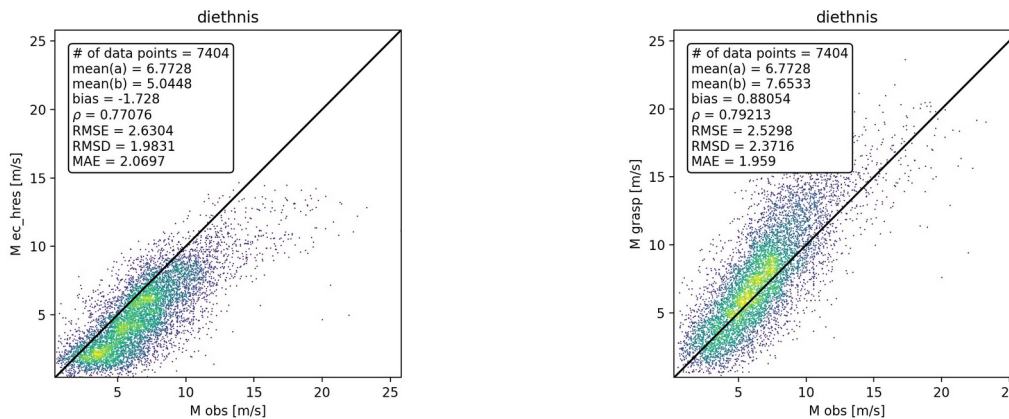
Figure 32: Scatter plots of ECMWF (left) and GRASP (right) vs. SCADA hourly mean wind speeds for the Diethnis wind farm.

Results Scatter plots and error metrics for the Diethnis wind farm are shown in Figure 32. The ECMWF wind speed shows a clear underestimation of wind speed with an overall bias: 1.7 m/s. GRASP on the other hand overestimates wind speeds (with a bias of 0.9 m/s), and the scatter plot shows that the overestimation becomes larger for large wind speeds. In bias sensitive error metrics RMSE and MAE, GRASP shows an improvement compared to ECMWF. This is also the case for the correlation coefficient, but not for the RSMD. Potentially, additional filtering (smoothing) of the GRASP signal would improve the RMSD score.

DehAnanewsimes and Eurowind Compared to the other two Rhodos sites, the DehAnanewsimes and Eurowind wind farm sites are in somewhat lower mountains close to the coast. Simulation details for the DehAnanewsimes and Eurowind windfarms are given in Appendix A.

Setup The domain size is chosen as 15.4km x 15.4km. Further domain settings can be found in Appendix A. The wind farm situation, surrounding orography and land cover can be seen in Figure 33.
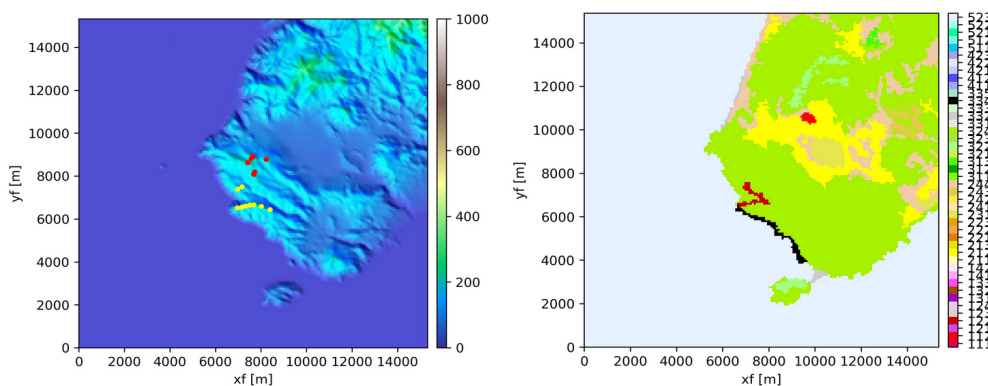
Figure 33: Height map and land use of the DehAnanewsimes and Eurowind domain.

Results Results of the DehAnanewsimes wind farm, located roughly 1.5 km from the coast on a 300m hill, case are summarized in Figure 34, which shows scatter plots and error metrics of GRASP and ECMWF against the SCADA observations. On all error metrics, GRASP shows a consistent improvement w.r.t. ECWMF. However, GRASP still shows a significant bias (underprediction) of 0.73 m/s, which is present accros the entire wind speed range.

(a) ECMWF vs. SCADA   **(b) GRASP vs. SCADA**
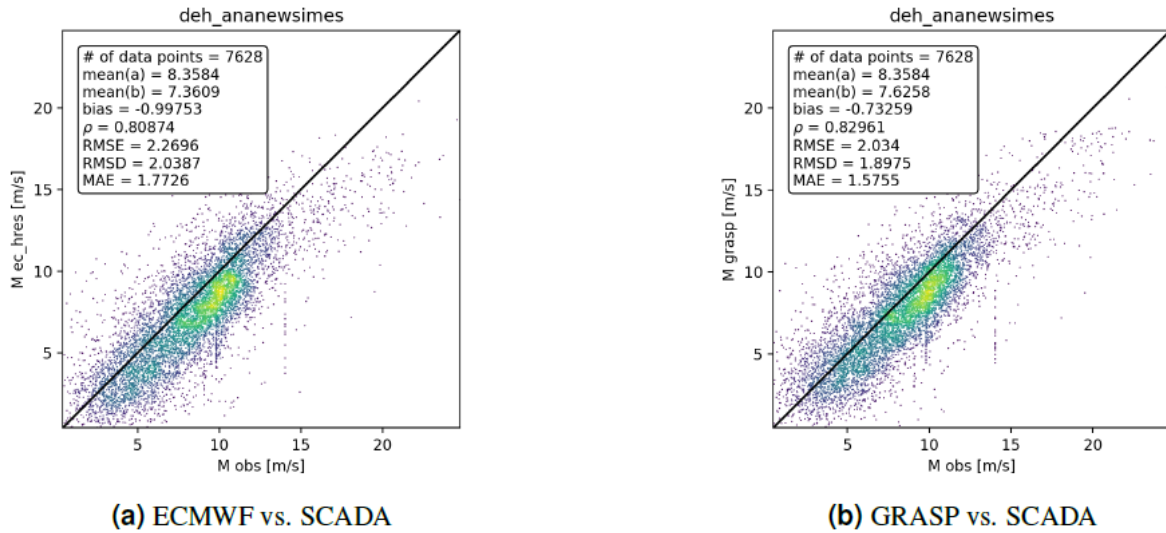
Figure 34: Scatter plots of ECMWF and GRASP vs. SCADA hourly mean wind speeds for the DehAnanewsimes wind farm.

Results for the Eurowind wind farm, located within a kilometer from the coast, are presented in Figure 35. The results are similar to those of the nearby DehAnanewsimes windfarm: GRASP improves on all error metrics compared to ECMWF. In fact, the relative improvements are even larger than in the DehAnanewsimes case. Also, GRASP captures the general wind climate well, but has a bias of 0.38 m/s (underprediction).

(a) ECMWF vs. SCADA wind speed   **(b) GRASP vs. SCADA**
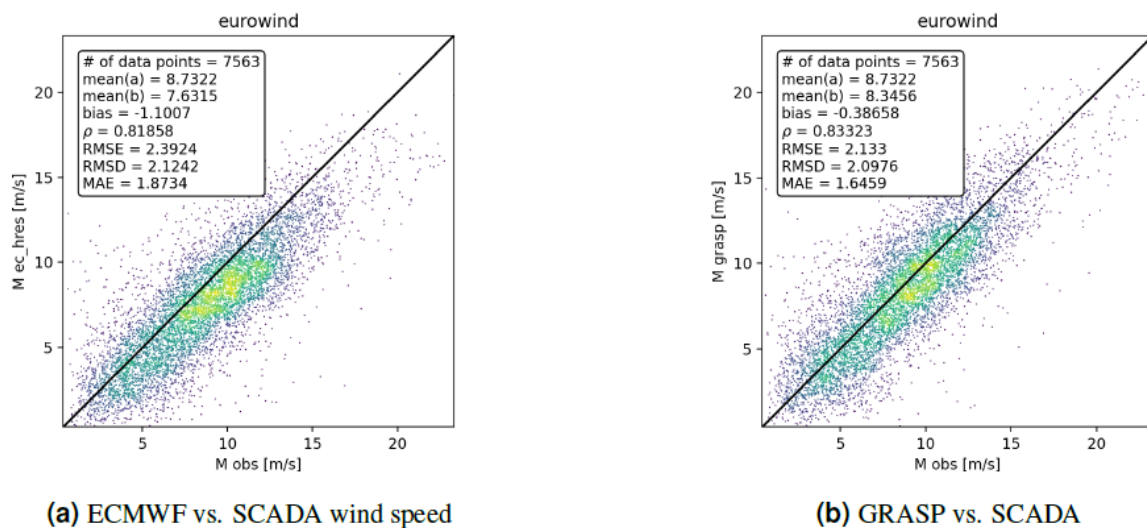
Figure 35: Scatter plots of ECMWF and GRASP vs. SCADA hourly mean wind speeds for the Eurowind wind farm.

La haute Borne

The La Haute Borne wind farm in the Meuse region in France consists of 4 Senvion MM82 wind turbines. It is one of the few wind farms for which the wind turbine SCADA data is made available to the general public (https://opendata-renewables.engie.com/explore/dataset/01c55756-5cd6-4f60-9f63-2d771bb25a1a/information).

The aim of this case study was to compare the forecast skill of GRASP vs. ECMWF forecasts. However, due to nonavailability of consecutive ECMWF historical data in a time period corresponding to the SCADA period, we chose to do the comparison based on ERA5 reanalysis data. To this end, we performed a 1-year (2015) LES run of La Haute Borne with ERA5 boundary conditions. Therefore, in the context of forecasting, the skill improvement of GRASP demonstrated here should be interpreted with caution.

Run setup The LES domain for La Haute Borne wind farm covers 8.2km x 8.2km. Figure 36 shows the layout of the wind farm, the orography and Corine land cover within the chosen domain. An overview of the additional domain settings is given in Appendix A.

(a) Height map of the La Haute Borne domain   (b) Corine land cover of the La Haute Borne domain
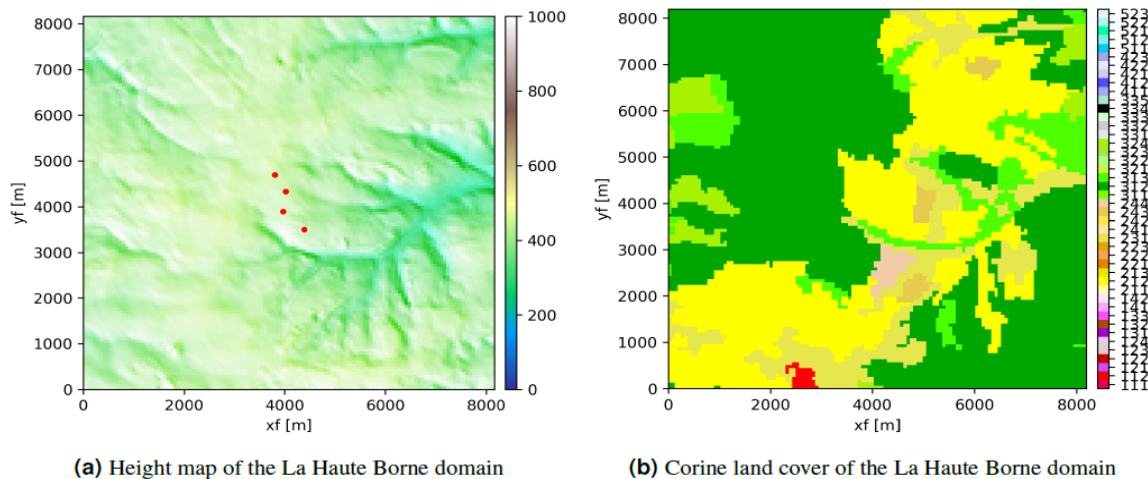
Figure 36: Height map and land use of the La Haute Borne domain.

Results The results of the run for La Haute Borne wind farm are summarized in Figure 37 by comparing both GRASP and ERA5 to the observations. From the scatter plots it can be observed that the GRASP wind speed resembles the observations better than the ERA5 data. This is reflected in the lower bias-sensitive error scores RMDE and MAE. In terms of RMSD GRASP is not matching ERA5, which can potentially be overcome by doing an additional filtering of the GRASP signal.

(a) ERA5 vs. SCADA
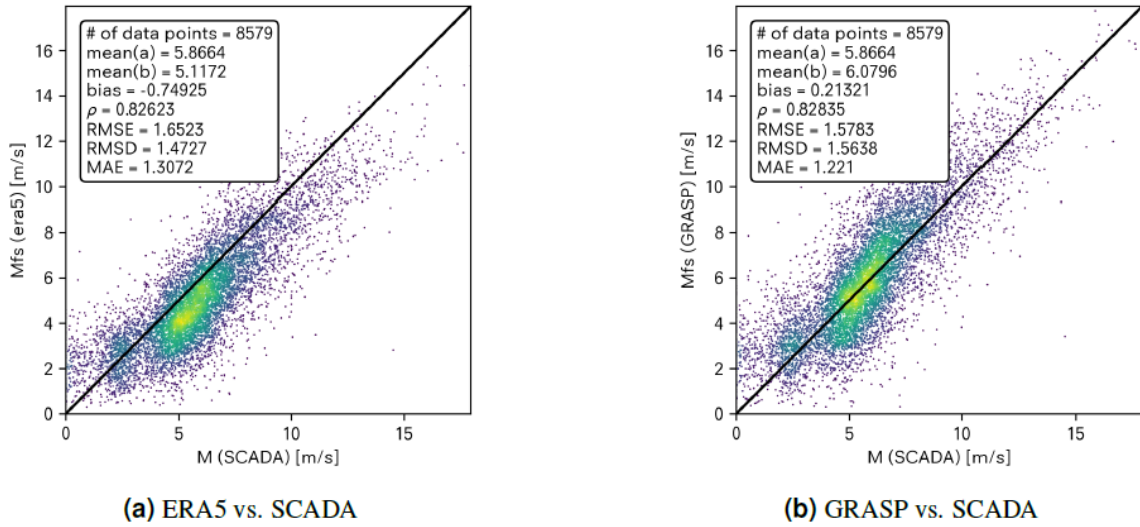
(b) GRASP vs. SCADA

Figure 37: Scatter plots of ERA5 and GRASP vs. SCADA hourly mean wind speeds of turbine R80711 at La Haute Borne wind farm.

Portuguese sites

EDP operates a number of wind farms in Portugal, of which the SCADA data has been made available for Smart4RES project partners. As with previous case studies, the aim is to investigate the forecast skill of GRASP vs. The ECMWF forecasts. We performed a 1-year (2018) run for 2 of the 11 Portuguese sites, using ECMWF high resolution BC, and compared the results to SCADA data. The run setup and results for Bairro and Tocha will be discussed in the next paragraphs.

Bairro Bairro wind farm is located in the Santarem district and consists of 11 Enercon E82 wind turbines.

Run setup The LES domain for Bairro wind farm covers 10.2km x 10.2km. Figure 38 shows the layout of the wind farm, the orography and Corine land cover within the chosen domain. An overview of the additional domain settings is given in Appendix A.

(a) Height map of the Bairro domain

(b) Corine land cover of the Bairro domain
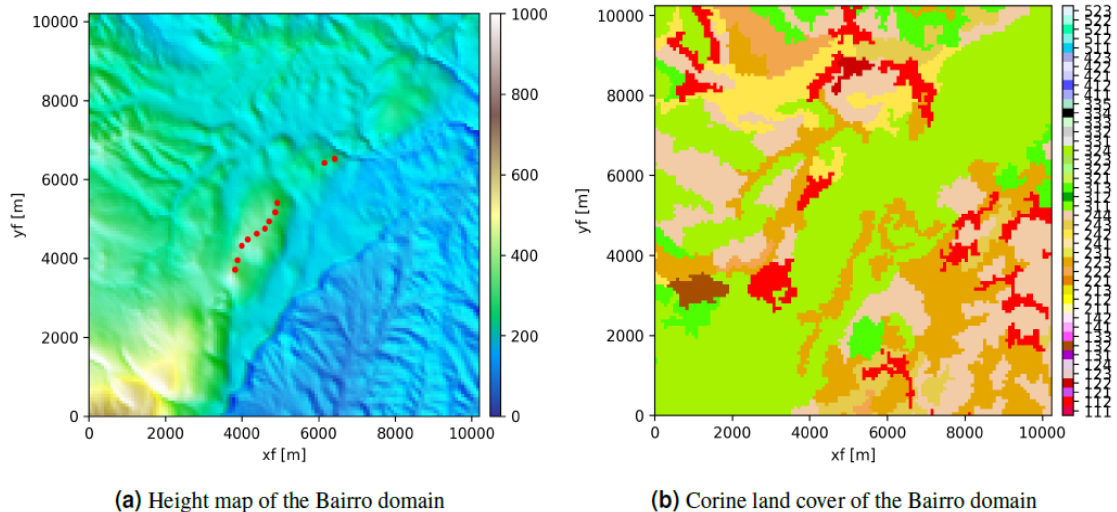
Figure 38: Height map and land use of the Bairro domain.

Results The results of the run for Bairro wind farm are summarized in Figure 39. It is observed that GRASP has a larger bias and therefore larger RMSE and MAE values. Also the RMSD of GRASP is higher than that of ECMWF. A clear cause for the overestimation of the wind speed has not been identified and would require further research. One hypothesis is that pre-cursor wind speeds (nudged towards ECMWF values), that are applied on the boundaries of the cursor domain, lead to an unrealistic speed-up over the mountain ridges.
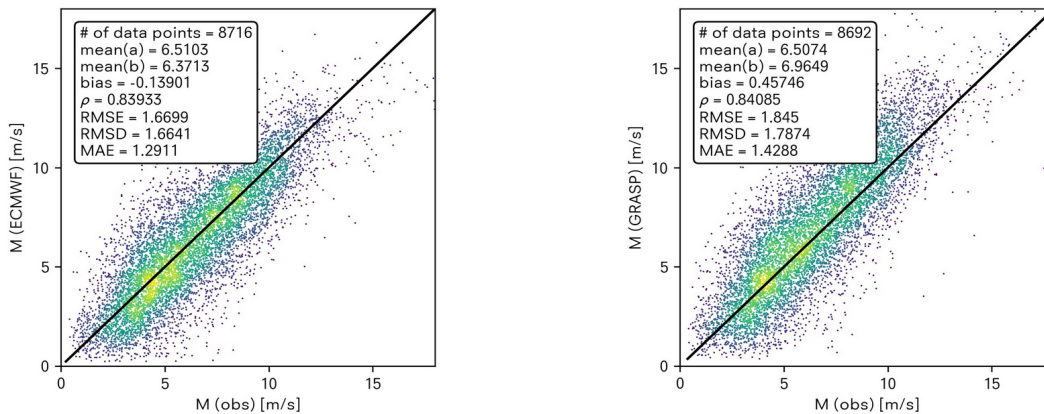
Figure 39: Scatter plots of ECMWF (left) and GRASP (right) vs. SCADA hourly mean wind speeds for Bairro wind farm.

Tocha Tocha wind farm is located in the Coimbra district and consists of 5 Vestas V100 wind turbines.

Run setup The LES domain for Tocha wind farm covers 10.2m x 10.2km. Figure 40 shows the layout of the wind farm, the orography and Corine land cover within the chosen domain. An overview of the additional domain settings is given in Appendix A.
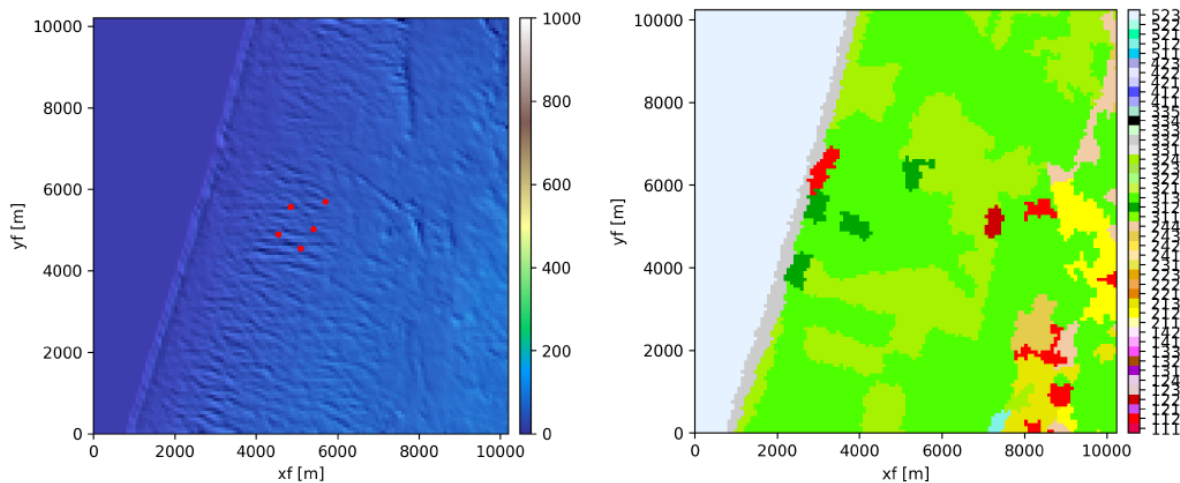

(a) Height map of the Tocha domain

(b) Corine land cover of the Tocha domain

Figure 40: Height map and land use of the Tocha domain.
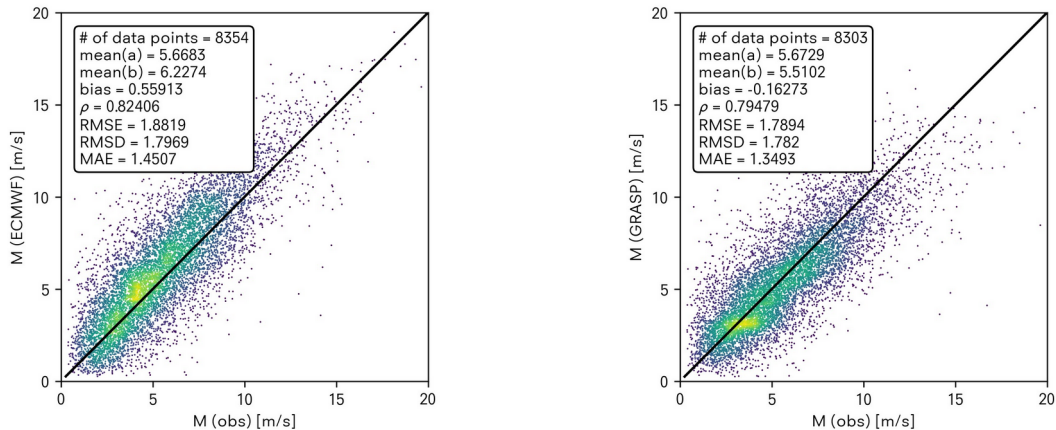
Figure 41: Scatter plots of ECMWF(left) and GRASP (right) vs. SCADA hourly mean wind speeds for Tocha wind farm.

Results Figure 41 shows the results of the run for Tocha wind farm. Comparing GRASP to ECMWF it is observed that GRASP reduces the bias and error scores. Also the RMSD is reduced in the GRASP forecast. The correlation coefficient from the GRASP data is lower than that of ECMWF. More research is required to determine the cause for this, but in Gilbert et al., 2020 it was shown that time-filtering (smoothing) the GRASP signal can lead to a higher correlation coefficient.

Oldenburg

The Oldenburg region in Germany is of interest for Smart4RES because it has a unique measurement infrastructure for solar radiation purposes consisting of all-sky cameras and other radiation measurements. Meteorologically, it is a challenging site due to the land-sea transition that can give rise to small-scale phenomena. As an illustration, Figure 42 shows the forecasted and observed cloud field on 21-07-2021, a summer day in which convective clouds devevelop over land. A visual comparison between the GRASP cloud field and the satellite image demonstrates the GRASP skill in a qualitative manner. The actual run settings and results for the Oldenburg site will be part of another deliverable within the Smart4RES project.
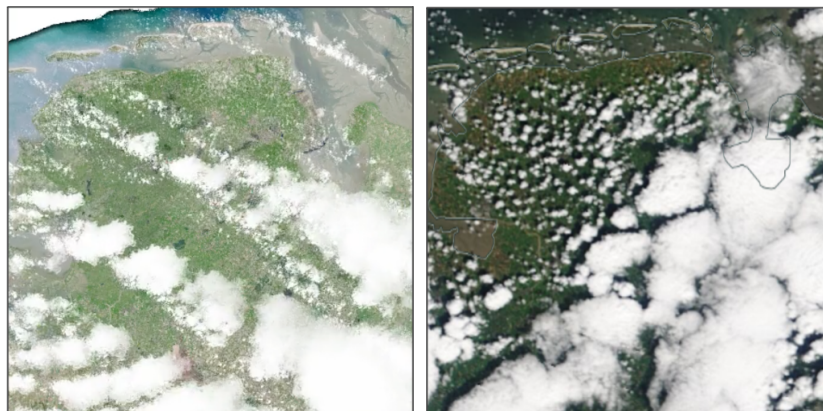
Figure 42: Comparison of forecasted and observed cloud field for the Oldenburg region for 2020-07-21.

Conclusions

The materials presented in this document show how high-resolution weather forecasting with LES can contribute to RES forecasting needs. We gave a concise description of the governing equations and a high-level description of the relevant physics modules for RES forecasting. Case studies for a selection of wind farms in Rhodes, France and Portugal have been presented. In the results, we focus on a comparison with the ECMWF forecasts, which provide a useful industry benchmark and are also the large-scale boundary conditions for the GRASP forecasts.

Results show that for most sites, GRASP hourly averaged error metrics improve with respect to those of the ECMWF model. The improved error metrics are mostly the consequence of GRASP's ability to represent a local wind climate better. This results in a lower bias and as a consequence an improvement of bias-sensitive skill scores. For some sites, the hourly average GRASP forecasts have slightly higher errors than the ECMWF forecasts. A clear cause for this has not been identified. In addition to lower errors of hourly averaged quantities, GRASP output shows realistic high-frequency variance associated with turbulent fluctuations. Results showed that small-scale turbulent fluctuations with a timescale lower than 15 minutes are accurately captured. Meso-scale fluctuations with time-scales between roughly 15 minutes and an hour are underestimated. This could be the consequence of the simulation set-up with a domain that is too small to generated meso-scale dynamics.

Further research is recommended to investigate the sources of error in GRASP. Conditioning wind forecast errors on weather conditions and terrain characteristics could provide more insights in the model errors. Such insights will also inform where model improvements can be realised, for example in the handling of the lateral boundary conditions, the lower boundary conditions and the representation of terrain and vegetation or the sub-grid model formulation.

Conclusion

In this report we have presented an evaluation of the high-resolution NWP models run for the Smart4RES project.

Kilometre-scale Arome-EPS forecasts developed by Météo-France show improvements over the currently operational configuration, for both 100-meter wind speed and global solar irradiance. The improvements come from the combined effect of increased spatial resolution, increased number of forecasts, and a valuable information on the rapid variations of wind and irradiance. A more thorough evaluation using a larger set of observations should be performed in future work to confirm these first results.

Météo-France is planning to upgrade the current Arome-EPS spatial resolution mid-2022. This will thus allow the RES sector to benefit from the improvements highlighted in this document in the next few months.

The performance gain provided by the enhanced Arome-EPS allows to reach the lower bound of the project KPIs. However, several avenues for improvement are currently being investigated to further improve the performance and achieve or even beat the higher bound of the KPIs. These contributions focus on refinements of the Arome model physics and uncertainty representation, and should be put into operations within the next 2 years.

LES simulations driven by ECMWF forecasts run by Whiffle for several wind farms also indicated an enhanced ability to represent the local wind, compared to the reference ECMWF forecasts. For the considered sites, the average improvement over the ECMWF baseline constitutes 9% for mean absolute error.

Whiffle is currently implementing a number of improvements that could reduce errors further. The most important ones are 1) an improved method to apply the large-scale boundary conditions from ECMWF in strongly heterogeneous terrain 2) multi-GPU functionality to allow larger computational domains and 3) data assimilation to improve the short-term forecast skill.

Key messages

- High-resolution ensemble NWP improves the forecast performance of wind and solar irradiance
- High-frequency outputs include a useful information information that could benefit to RES users
- LES forecasts outperforms state-of-the-art ECMWF NWP forecasts for the representation of local wind

References

Bianco, L., Djalalova, I. V., Wilczak, J. M., Cline, J., Calvert, S., Konopleva-Akish, E., & Freedman, J. (2016). A wind energy ramp tool and metric for measuring the skill of numerical weather prediction models. *Weather and Forecasting*, *31*(4), 1137-1156.

Böing, S. (2014). The interaction between deep convective clouds and their environment. PhD thesis, TU Delft.

Bouttier, F., Raynaud, L., Nuissier, O., & Ménétrier, B. (2016). Sensitivity of the AROME ensemble to initial and surface perturbations during HyMeX. Quarterly Journal of the Royal Meteorological Society, 142, 390-403.

De Roode S.R. (2012). Parameterization of the vertical velocity equation for shallow cumulus clouds. *Monthly Weather Review*, 140(8):2424–2436.

ECMWF (2017). IFS Manual Part IV: Physical Processes. IFS Documentation Cy43R3. Technical report, ECMWF.

Gilbert, C., Messner, J. W., Pinson, P., Trombe, P. J., Verzijlbergh, R., van Dorp, P., and Jonker, H. (2020). Statistical post-processing of turbulence-resolving weather forecasts for offshore wind power forecasting. *Wind Energy*, 23(4):884–897.

Hagelin, S., J. Son, R. Swinbank, A. McCabe, N. Roberts, and W. Tennant, 2017 : The Met Office convective-scale ensemble MOGREPS-UK. Quart. J. Roy. Meteor. Soc., 143, 2846–2861.

Heus, T., Van Heerwaarden, C. C., Jonker, H. J. J., Siebesma, A. P., Axelsen, S., Van Den Dries, K., Geoffroy, O., Moene, A. F., Pino, D., De Roode, S. R., and Vila-Guerau de Arellano, J. (2010). Formulation of the Dutch Atmospheric Large-Eddy Simulation (DALES) and overview of its applications. *Geoscientific Model Development*, 3(2):415–444.

Hogan, R. J., & Bozzo, A. (2018). A flexible and efficient radiation scheme for the ECMWF model. *Journal of Advances in Modeling Earth Systems*, *10*(8), 1990-2008.

Descamps, L., Labadie, C., Joly, A., Bazile, E., Arbogast, P., & Cébron, P. 2015 : PEARP, the Météo-France short-range ensemble prediction system. Quarterly Journal of the Royal Meteorological Society, 141(690), 1671-1685.

Guorui Ren, Jinfu Liu , Jie Wan, Fei Li, Yufeng Guo, Daren Yu, 2018 : The analysis of turbulence intensity based on wind speed data in onshore wind farms, Renewable Energy, 123, 756-766.

Hämäläinen, K., Saltikoff, E., Hyvärinen, O., Vakkari, V., & Niemelä, S. (2020). Assessment of Probabilistic Wind Forecasts at 100 m Above Ground Level Using Doppler Lidar and Weather Radar Wind Profiles, *Monthly Weather Review*, *148*(3), 1321-1334. Retrieved Mar 17, 2022, from https://journals.ametsoc.org/view/journals/mwre/148/3/mwr-d-19-0184.1.xml

Meyers, J. and Meneveau, C. (2010). Large Eddy Simulations of Large Wind-Turbine Arrays in the Atmospheric Boundary Layer. *48th AIAA Aerospace Sciences Meeting Including the New Horizons Forum and Aerospace Exposition*, (January):1–10.

Raynaud, L., and F. Bouttier, 2017 : The impact of horizontal resolution and ensemble size for convective-scale probabilistic forecasts. Quart. J. Roy. Meteor. Soc., 143, 3037–3047.

Schalkwijk, J., Griffith, E. J., Post, F. H., and Jonker, H. J. J. (2012). High-performance simulations of turbulent clouds on a desktop PC. *Bulletin of the American Meteorological Society*, 93(3):307–314.

Schalkwijk, J., Jonker, H., Siebesma, A., and Van Meijgaard, E. (2015). Weather forecasting using GPU-based large-Eddy simulations. *Bulletin of the American Meteorological Society*, 96(5).

Benedikt Schulz, Mehrez El Ayari, Sebastian Lerch, Sándor Baran (2021). Post-processing numerical weather prediction ensembles for probabilistic solar irradiance forecasting, Solar Energy, Volume 220,
2021, Pages 1016-1031, ISSN 0038-092X, https://doi.org/10.1016/j.solener.2021.03.023.

Schwartz, C. S., and R. Sobash, 2017 : Generating probabilistic forecasts from convection allowing ensembles using neighborhood approaches : a review and recommendations. Monthly Weather Review, 145, 3397–3418.

Stevens, R. J., Graham, J., and Meneveau, C. (2014). A concurrent precursor inflow method for Large Eddy Simulations and applications to finite length wind farms. *Renewable Energy*, 68:46–50.

Stevens, R. J. and Meneveau, C. (2017). *Flow Structure and Turbulence in Wind Farms*, volume 49.

Tiggelen, M. V. (2018). Towards improving the land- surface-atmosphere coupling in the Dutch Atmospheric Large- Eddy Simulation model (DALES). Technical report, Delft University of Technology.

Wilks, D. S.: Statistical methods in the atmospheric sciences, Aca-demic press, 1995.

Wimmer M., L. Raynaud, L. Descamps, L. Berre and Y. Seity (2021) Sensitivity analysis of the convective-scale AROME model to physical and dynamical parameters. Quart. J. Roy. Meteor. Soc.

Wimmer M., 2021: Représentation de l'erreur de modélisation dans le système de prévision d'ensemble régional Arome-EPS. Thèse de doctorat de l'Université Toulouse 3 Paul Sabatier.

Worsnop, R. P., Scheuerer, M., Hamill, T. M., and Lundquist, J. K. (2018) : Generating wind power scenarios for probabilistic ramp event prediction using multivariate statistical post-processing, Wind Energ. Sci., 3, 371–393, https://doi.org/10.5194/wes-3-371-2018.

ICOS wind measurements:

Chen, H., Scheeren, B., ICOS RI, 2020. ICOS ATC Meteo Release, Lutjewad (60.0 m), 2019-01-10–2020-05-31, https://hdl.handle.net/11676/WtjMcUCWBiX30KMNJ8uAo_T8

Ramonet, M., Conil, S., Delmotte, M., Laurent, O., ICOS RI, 2020. ICOS ATC Meteo Release, Observatoire pérenne de l'environnement (10.0 m), 2016-08-18–2020-05-31, https://hdl.handle.net/11676/cUHMYjz1zy9ECO9cEkedkpQe

Ramonet, M., Conil, S., Delmotte, M., Laurent, O., ICOS RI, 2020. ICOS ATC Meteo Release, Observatoire pérenne de l'environnement (50.0 m), 2017-05-17–2020-05-31, https://hdl.handle.net/11676/Qs_Txxk0SfCZVY327fo9Hebd

Ramonet, M., Conil, S., Delmotte, M., Laurent, O., ICOS RI, 2020. ICOS ATC Meteo Release, Observatoire pérenne de l'environnement (120.0 m), 2016-08-18–2020-05-31, https://hdl.handle.net/11676/IxuPtWZm0afJ-IkMm9FgrM2Y

Ramonet, M., Lopez, M., Delmotte, M., ICOS RI, 2020. ICOS ATC Meteo Release, Trainou (50.0 m), 2016-11-03–2020-05-31, https://hdl.handle.net/11676/bp0E2hHVD-jrwr9eKKd0gyod

Ramonet, M., Lopez, M., Delmotte, M., ICOS RI, 2020. ICOS ATC Meteo Release, Trainou (180.0 m), 2017-03-06–2020-05-31, https://hdl.handle.net/11676/EjUQm7zj8Vz9itz2fGebS9re

Ramonet, M., Delmotte, M., ICOS RI, 2020. ICOS ATC Meteo Release, Saclay (40.0 m), 2017-11-09–2020-01-13, https://hdl.handle.net/11676/SGPRYaZ9z78qfPsumR1IYXRg

Ramonet, M., Delmotte, M., ICOS RI, 2020. ICOS ATC Meteo Release, Saclay (60.0 m), 2017-05-31–2020-05-31, https://hdl.handle.net/11676/RH21ZBRWcBTfzCjQmZJqXrpW

Ramonet, M., Delmotte, M., ICOS RI, 2020. ICOS ATC Meteo Release, Saclay (80.0 m), 2017-11-09–2020-01-13, https://hdl.handle.net/11676/RTeKB3YQcghXE8PnZiMU1SHt

Ramonet, M., Delmotte, M., ICOS RI, 2020. ICOS ATC Meteo Release, Saclay (100.0 m), 2017-05-31–2020-05-31, https://hdl.handle.net/11676/WURtkza_ZPcijZrbtZxki5Rm

Kubistin, D., Plaß-Dülmer, C., Arnold, S., Lindauer, M., Müller-Williams, J., Schumacher, M., ICOS RI, 2020. ICOS ATC Meteo Release, Gartow (30.0 m), 2016-05-10–2020-05-31, https://hdl.handle.net/11676/bP5viEekoyTUK2vvMf9jU5pE

Kubistin, D., Plaß-Dülmer, C., Arnold, S., Lindauer, M., Müller-Williams, J., Schumacher, M., ICOS RI, 2020. ICOS ATC Meteo Release, Gartow (60.0 m), 2016-05-10–2020-05-31, https://hdl.handle.net/11676/WZf6xBVK-N2Obk45OEAixQZw

Kubistin, D., Plaß-Dülmer, C., Arnold, S., Lindauer, M., Müller-Williams, J., Schumacher, M., ICOS RI, 2020. ICOS ATC Meteo Release, Gartow (132.0 m), 2016-05-10–2020-05-31, https://hdl.handle.net/11676/D3KtTWb2aNT3ZiWUTMuAWbd4

Kubistin, D., Plaß-Dülmer, C., Arnold, S., Lindauer, M., Müller-Williams, J., Schumacher, M., ICOS RI, 2020. ICOS ATC Meteo Release, Hohenpeissenberg (131.0 m), 2015-09-18–2020-05-31, https://hdl.handle.net/11676/Tjat6ZhMF0dM_XkTdU0Oc3CH

Kubistin, D., Plaß-Dülmer, C., Arnold, S., Lindauer, M., Müller-Williams, J., ICOS RI, 2020. ICOS ATC Meteo Release, Karlsruhe (30.0 m), 2019-08-01–2020-05-31, https://hdl.handle.net/11676/4Thj8jrq2waG8f-ohTkG2lBX

Kubistin, D., Plaß-Dülmer, C., Arnold, S., Lindauer, M., Müller-Williams, J., ICOS RI, 2020. ICOS ATC Meteo Release, Karlsruhe (60.0 m), 2019-08-01–2020-05-31, https://hdl.handle.net/11676/oxtJyFdByFJZStlltRETTDmz

Kubistin, D., Plaß-Dülmer, C., Arnold, S., Lindauer, M., Müller-Williams, J., ICOS RI, 2020. ICOS ATC Meteo Release, Karlsruhe (100.0 m), 2019-08-01–2020-05-31, https://hdl.handle.net/11676/25w0UeLR6PfUuNhmXFryg6L1

Kubistin, D., Plaß-Dülmer, C., Arnold, S., Lindauer, M., Müller-Williams, J., Schumacher, M., ICOS RI, 2020. ICOS ATC Meteo Release, Lindenberg (10.0 m), 2017-02-21–2020-05-31, https://hdl.handle.net/11676/RAkXxgu_ErHRfrE7pzmkX1gvKubistin, D., Plaß-Dülmer, C., Arnold, S., Lindauer, M., Müller-Williams, J., Schumacher, M., ICOS RI, 2020. ICOS ATC

Meteo Release, Lindenberg (40.0 m), 2017-02-21–2020-05-31, https://hdl.handle.net/11676/V7bVeYaDHI2PgrFsjMonzrNc

Kubistin, D., Plaß-Dülmer, C., Arnold, S., Lindauer, M., Müller-Williams, J., Schumacher, M., ICOS RI, 2020. ICOS ATC Meteo Release, Lindenberg (98.0 m), 2017-02-21–2020-05-31, https://hdl.handle.net/11676/97cvwGnOhROLFuFhw7yB1dmq

Kubistin, D., Plaß-Dülmer, C., Arnold, S., Lindauer, M., Müller-Williams, J., ICOS RI, 2020. ICOS ATC Meteo Release, Ochsenkopf (163.0 m), 2019-09-25–2020-05-31, https://hdl.handle.net/11676/XPI_SZj8IOcniNJ5qin_y4bM

Kubistin, D., Plaß-Dülmer, C., Arnold, S., Lindauer, M., Müller-Williams, J., ICOS RI, 2020. ICOS ATC Meteo Release, Steinkimmen (32.0 m), 2019-07-22–2020-05-31, https://hdl.handle.net/11676/jCpqodP8QhFALSUQPqkZTINF

Kubistin, D., Plaß-Dülmer, C., Arnold, S., Lindauer, M., Müller-Williams, J., ICOS RI, 2020. ICOS ATC Meteo Release, Steinkimmen (82.0 m), 2019-07-22–2020-05-31, https://hdl.handle.net/11676/sZjdgQvUJX2KsBe7CHx2drty

Kubistin, D., Plaß-Dülmer, C., Arnold, S., Lindauer, M., Müller-Williams, J., ICOS RI, 2020. ICOS ATC Meteo Release, Steinkimmen (127.0 m), 2019-07-22–2020-05-31, https://hdl.handle.net/11676/X4mSv_Y6va09SMlrURAwApKd

Kubistin, D., Plaß-Dülmer, C., Arnold, S., Lindauer, M., Müller-Williams, J., ICOS RI, 2020. ICOS ATC Meteo Release, Steinkimmen (187.0 m), 2019-07-22–2020-05-31, https://hdl.handle.net/11676/w1xEApXVf6rO9nMPRuiwoCDo

Kubistin, D., Plaß-Dülmer, C., Arnold, S., Lindauer, M., Müller-Williams, J., Schumacher, M., ICOS RI, 2020. ICOS ATC Meteo Release, Torfhaus (10.0 m), 2018-01-01–2020-05-31, https://hdl.handle.net/11676/qQkl2hpPHCNTRms1wOTafy7D

Kubistin, D., Plaß-Dülmer, C., Arnold, S., Lindauer, M., Müller-Williams, J., Schumacher, M., ICOS RI, 2020. ICOS ATC Meteo Release, Torfhaus (76.0 m), 2018-01-01–2020-05-31, https://hdl.handle.net/11676/AX21BZkNPUDCz9-avOPf1LUr

Kubistin, D., Plaß-Dülmer, C., Arnold, S., Lindauer, M., Müller-Williams, J., Schumacher, M., ICOS RI, 2020. ICOS ATC Meteo Release, Torfhaus (110.0 m), 2018-06-21–2020-05-31, https://hdl.handle.net/11676/MdUw88Bj6uQjrS9SgBrglOAr

Kubistin, D., Plaß-Dülmer, C., Arnold, S., Lindauer, M., Müller-Williams, J., Schumacher, M., ICOS RI, 2020. ICOS ATC Meteo Release, Torfhaus (147.0 m), 2018-01-01–2020-05-31, https://hdl.handle.net/11676/wWZqDB48i3P6cj0WFMjw9O0BBergamaschi, P., Manca, G., ICOS RI, 2020. ICOS ATC Meteo Release, Ispra (40.0 m), 2017-12-10–2020-05-31, https://hdl.handle.net/11676/s9AnWH5xYmXNdezOLgfF2fAh

Bergamaschi, P., Manca, G., ICOS RI, 2020. ICOS ATC Meteo Release, Ispra (100.0 m), 2017-12-10–2020-05-31, https://hdl.handle.net/11676/AtDUlm5CeNuYR-7mJ6G7aw1o

SOFOG3D wind measurements:

Canut, G., & Garrouste, O. (2020). SOFOG3D_TUZAN_CNRM_MTO-1MIN_L2. Aeris. https://doi.org/10.25326/99

Canut, G., & Garrouste, O. (2020). SOFOG3D_NIZAN_CNRM_MTO-1MIN_L2. Aeris. https://doi.org/10.25326/100

A Appendix: LES domain settings

Diethnis

	Precursor	Run 1
Δ_x	80m	80m
Δ_y	80m	80m
Δ_z	20m	20m
L_x	15360m	15360m
L_y	15360m	15360m
L_z	2560m	2560m
lat centre	36.2458	36.2458
lon centre	28.0554	28.0554

Aeiforiki

	Precursor	Run 1
Δ_x	80m	80m
Δ_y	80m	80m
Δ_z	20m	20m
L_x	15360m	15360m
L_y	15360m	15360m
L_z	2560m	2560m
lat centre	36.0358	36.0358
lon centre	27.8190	27.8190

DehAnanewsimes and Eurowind

	Precursor	Run 1
Δ_x	80m	80m
Δ_y	80m	80m
Δ_z	20m	20m
L_x	15360m	15360m
L_y	15360m	15360m
L_z	2560m	2560m
lat centre	35.9287	35.9287
lon centre	27.7456	27.7456

La Haute Borne

	Precursor	Run 1
Δ_x	64m	64m
Δ_y	64m	64m
Δ_z	16m	16m
L_x	8192m	8192m
L_y	8192m	8192m
L_z	4118m	2558m
lat centre	48.4461	48.4461
lon centre	5.5925	5.5925

Bairro

	Precursor	Run 1
Δ_x	80m	80m
Δ_y	80m	80m
Δ_z	20m	20m
L_x	10240m	10240m
L_y	10240m	10240m
L_z	2560m	2560m
lat centre	39.590	39.590
lon centre	-8.570	-8.570

Tocha

	Precursor	Run 1
Δ_x	80m	80m
Δ_y	80m	80m
Δ_z	20m	20m
L_x	10240m	10240m
L_y	10240m	10240m
L_z	2560m	2560m
lat centre	40.319	40.319
lon centre	-8.817	-8.817